# DISCONTINUOUS GALERKIN GALERKIN DIFFERENCES FOR THE WAVE EQUATION IN SECOND-ORDER FORM\*

J. W. BANKS<sup>†</sup>, B. BRETT BUCKNER<sup>†</sup>, T. HAGSTROM<sup>‡</sup>, AND K. JUHNKE<sup>§</sup>

**Abstract.** We develop interior penalty discontinuous Galerkin difference methods for the wave equation in second-order form. The new schemes are energy conserving or energy dissipating depending on the simple choice of centered or upwind fluxes and are superconvergent away from boundaries. Unlike analogous methods using standard piecewise polynomial bases, we find that no mesh-dependent penalty parameters are needed to guarantee stability and time step stability constraints for explicit time-marching have a mild dependence on method order. Basic properties of the proposed discretizations are illustrated with numerical experiments in one and two space dimensions.

Key words. difference methods, Galerkin methods, wave equation

AMS subject classifications. 65M60, 65M06

**DOI.** 10.1137/20M1328671

1. Introduction. Galerkin differences (GD) [4, 5, 14] are a relatively new class of finite element approximation based on Galerkin projection into a piecewise polynomial space. Unlike traditional FEM, however, high-order polynomial representations are obtained without the introduction of new degrees of freedom (DoFs) and instead use neighboring DoFs define the polynomial approximation over a given element. In this way, the underlying discrete space is defined using profitable ideas from the finite difference literature, while the overall approach retains many benefits of having built the discretization around a Galerkin projection of the weak form of the equations. In particular, away from the boundaries the method yields a uniform compact difference stencil similar to a compact or Padé-type scheme [17]. At the same time, since the approach is of finite element type, standard arguments can be used to show energy stability. The end result is a scheme with excellent properties, e.g., time step restrictions that grow only slowly (or not at all) as the order of the method is increased, and superconvergence behavior at grid points, e.g., [4, 5] show order  $\mathcal{O}(h^{2p})$  where p is the order of the polynomial reconstruction.

Upwind numerical methods are commonly employed in the solution of hyperbolic PDEs due to the presence of natural dissipation induced by the construction. This is typically achieved by incorporating characteristic information from the PDE into the numerical method, often by imposing the exact or approximate solution to a Riemann problem at cell or element boundaries. Upwind dissipation has been extremely useful, particularly for hyperbolic PDEs. For example, in nonlinear conservation laws,

<sup>\*</sup>Submitted to the journal's Methods and Algorithms for Scientific Computing section April 2, 2020; accepted for publication (in revised form) November 30, 2020; published electronically April 29, 2021.

https://doi.org/10.1137/20M1328671

**Funding:** This work was supported by contracts from the U.S. Department of Energy ASCR Applied Math Program, by a U.S. Presidential Early Career Award for Scientists and Engineers, and by NSF grants DMS-1418871 and DMS-2012296. Any opinions, findings, and conclusions or recommendations expressed in this material are those of the authors and do not necessarily reflect the views of the Department of Energy or the National Science Foundation.

<sup>&</sup>lt;sup>†</sup>Rensselaer Polytechnic Institute, Troy, NY 12180 USA (banksj3@rpi.edu, bucknb2@rpi.edu).

<sup>&</sup>lt;sup>‡</sup>Department of Mathematics, Southern Methodist University, Dallas, TX 75205 USA (thagstrom@mail.smu.edu).

<sup>§</sup>Bethel College, North Newton, KS 67117 USA (kjuhnke@bethelks.edu).

shocks are known to form in finite time even from smooth initial data, and upwind dissipation is found to naturally stabilize numerical approximations. Similarly, for problems with discontinuous material coefficients, upwind dissipation has been profitably applied in order to reduce or remove unphysical high-frequency oscillations in the solution. In these (and other) examples, numerical dissipation is added naturally based on the formulation of the upwind method without the need for user intervention via tunable parameters. Classical upwind schemes include many powerful approaches such as Godunov's method and its extension [11, 2], flux-corrected transport [7], semi-Lagrangian methods [24], the piecewise-parabolic method [9], essentially nonoscillatory schemes [13], weighted essentially nonoscillatory methods [15], and discontinuous Galerkin (DG) methods [8].

The amalgamation of finite elements and upwind methods are DG methods, which are finite element methods in which continuity is not imposed at the boundaries between elements. There are many advantages to DG methods, one of which is that the flux at element boundaries, which arises after integration by parts over each element, provides a natural algorithmic hook where characteristic information from the PDE can be incorporated to yield an upwind method. When applied to wave equations, there are essentially two approaches in the literature for upwind DG methods. The most common is conversion into a system of first-order PDEs so that classical DG methods can be applied. However, this approach can have drawbacks including the fact that conversion to first-order form typically introduces new dependent variables and compatibility constraints that are needed to ensure equivalence of solutions from the first- and second-order forms of the equations. The second approach, first described in [1], retains the second-order form of the equations but uses a nonstandard approach that tests against the derivative of the Lagrangian of the test function, rather than the test function itself.

The current paper introduces an upwind DG-like method for the second-order wave equation within the GD framework. This new scheme takes the form of an interior penalty Galerkin (IPG) method, and both symmetric and incomplete interior penalty methods [23] (called SIPGD and IIPGD, respectively) are considered. The IPG formulation enables stable discretization of the Laplacian without the need for conversion to first-order form or testing against the Lagrangian. Natural choices for the numerical flux at element boundaries yield either a centered dissipation-free discretization or an upwind-style scheme with natural dissipation. For the latter, the core development from [6] is applied, which embeds the solution of a local Riemann-like problem at the element faces to determine an upwind flux that is compatibile with the IPG formulations. The resulting schemes are high-order accurate and energy stable and are found to have only minor time step restrictions as the order of accuracy increases. The SIPGD scheme also exhibits superconvergence at the grid points of order  $\mathcal{O}(h^{2p})$  as in [4].

GD methods have some similarities to methods which combine elementwise variational formulations with polynomial approximations computed on an extended collection of neighboring elements, as in the least squares reconstruction of [10], or the (global) variational reconstruction of [18] which is used to compute the fluxes. However, these methods differ from GD in that they abandon the Galerkin framework to avoid a globally connected mass matrix. In the present work we are able to retain the advantages of a true Galerkin formulation and leverage a tensor-product mesh to maintain linear complexity when applying the inverse mass matrix. One disadvantage of our approach is that its extension to fully unstructured meshes may involve inversion of mass matrices without a tensor-product structure, although extension to

block-structured or mapped grids is still possible.

The structure of this paper is as follows. Section 2 discusses the construction of the discontinuous basis functions in the GD framework. Section 3 explains the discretization of the wave equation, the determination of the upwind flux, the treatment of boundary conditions, and the extension to higher dimensions. Section 4 gives an analysis of the scheme, including an energy estimate, dispersion analysis that demonstrates the superconvergence of the scheme at the grid points, and spectral computations that verify the stability and upwind properties of the discretization operators with boundary closures. Section 5 presents results verifying the convergence properties and demonstrating the robustness of the various schemes applied to classical and nonclassical problems. Some concluding remarks are given in section 6. Finally Appendix A provides a discussion of the coercivity of the bilinear operator.

2. Basis functions. As in prior GD work, the approximations discussed here are built around a piecewise polynomial interpolant, for which there exists a classical and well-known convergence theory. Unlike prior GD work, however, the interpolant here is built on a dual grid, which naturally leads to discontinuous reconstructions. Once the interpolation is defined, basis functions associated with DoFs can be derived following the basic approach outlined in [4, 5, 14]. The basis can then be used in a Galerkin discretization.

To describe the discontinuous basis used in this work, consider a uniform mesh in one space dimension defined by  $x_j = jh$ , with h being the mesh size, and  $j = \ldots, -1, 0, 1, \ldots$  Denote  $u_j \approx u(x_j)$  as the discrete approximation of the function u(x) at the grid points. A piecewise polynomial interpolant,  $\tilde{u}(x)$ , is then defined on the dual grid. Considering a generic interval on this dual grid,  $(x_{k-1/2}, x_{k+1/2})$ ,  $\tilde{u}(x)$  is defined to be the degree p polynomial interpolating the solution at the p+1 grid points  $x_{k-p/2}, \ldots, x_{k+p/2}$ . Note here that p is assumed even. The approximation on the interval  $(x_{k-1/2}, x_{k+1/2})$  is given by

(2.1) 
$$\tilde{u}(x) = \sum_{j=k-p/2}^{k+p/2} u_j l_j^{(p)}(x),$$

where  $l_j^{(p)}(x)$  is the Lagrange basis polynomial of degree p. It is clear that each  $u_j$  appears as a linear coefficient in exactly p+1 intervals surrounding  $x_j$ . Therefore, basis functions  $\phi_j^{(p)}(x)$ , associated with each DoF, can be derived so that

(2.2) 
$$\tilde{u}(x) = \sum_{j=-\infty}^{\infty} u_j \phi_j^{(p)}(x),$$

with  $\phi_j^{(p)}(x)$  nonzero over p+1 intervals surrounding  $x_j$ . For example, formulas for the degree two and four basis functions are given in (2.3) and (2.4), respectively,

(2.3) 
$$\phi_j^{(2)}(\xi_j) = \begin{cases} \frac{(\xi_j + 2h)(\xi_j + h)}{2h^2}, & -3h/2 < \xi_j \le -h/2, \\ -\frac{(\xi_j - h)(\xi_j + h)}{h^2}, & -h/2 < \xi_j \le h/2, \\ \frac{(\xi_j - h)(\xi_j - 2h)}{2h^2}, & h/2 < \xi_j \le 3h/2, \\ 0 & \text{else}, \end{cases}$$

$$(2.4) \qquad \phi_{j}^{(4)}(\xi_{j}) = \begin{cases} \frac{(\xi_{j}+4h)(\xi_{j}+3h)(\xi_{j}+2h)(\xi_{j}+h)}{24h^{4}}, & -5h/2 < \xi_{j} \leq -3h/2, \\ -\frac{(\xi_{j}+3h)(\xi_{j}+2h)(\xi_{j}+h)(\xi_{j}-h)}{6h^{4}}, & -3h/2 < \xi_{j} \leq -h/2, \\ \frac{(\xi_{j}+2h)(\xi_{j}+h)(\xi_{j}-h)(\xi_{j}-2h)}{4h^{4}}, & -h/2 < \xi_{j} \leq h/2, \\ -\frac{(\xi_{j}+h)(\xi_{j}-h)(\xi_{j}-2h)(\xi_{j}-3h)}{6h^{4}}, & h/2 < \xi_{j} \leq 3h/2, \\ \frac{(\xi_{j}-h)(\xi_{j}-2h)(\xi_{j}-3h)(\xi_{j}-4h)}{24h^{4}}, & 3h/2 < \xi_{j} \leq 5h/2, \\ 0 & \text{else,} \end{cases}$$

where  $\xi_j = x - x_j$  and  $x_j$  is the grid point at the center. In addition, plots of the basis and its derivative are given for p = 2, 10, and 100 in Figure 2.1. Note that because each basis function spans nearby elements, modifications must be applied near domain boundaries, and such modifications will be discussed later as appropriate.

The basis functions  $\phi_j^{(p)}$  have a number of interesting and useful properties. Clearly the basis has jumps at the points  $x_{j\pm 1/2}$ , and so the derivative must formally contain delta functions at each  $x_{j\pm 1/2}$ . Nevertheless, the limits of the derivative from the left and right are equal at all points, including  $x_{j\pm 1/2}$ . This can be seen in the plots of the derivative in Figure 2.1 and will be further discussed in Appendix A. As we shall see later in this paper, this implies that derivative values appearing in the fluxes are determined unambiguously. Furthermore, the decay of the basis functions away from the central point  $\xi_j = 0$  implies that the elements of the mass and stiffness matrices will also decay rapidly away from the diagonal. In fact, the compact support of the functions implies the mass and stiffness matrices will be banded with bandwidth 2p+1. We also note that like their continuous counterparts in [4], these basis functions approach sinc in the limit as  $p \to \infty$ , although the rate of convergence is slow; in particular the size of the jump at the discontinuity is O(1/p).

3. Semidiscretization of the wave equation and numerical fluxes. As in any finite element method, the basis described previously in section 2 can be used to discretize a PDE using a standard Galerkin projection approach. Since the basis

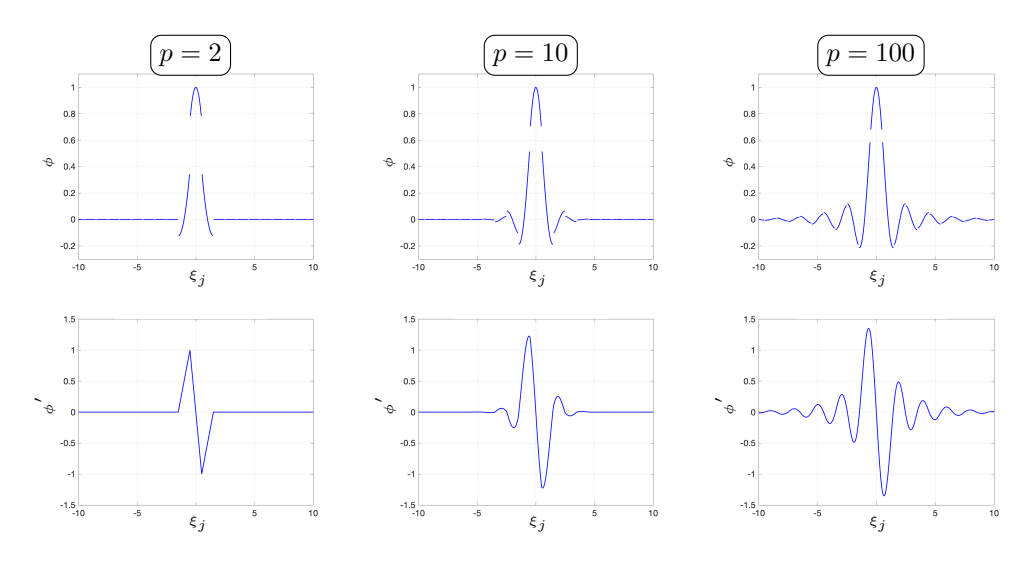


Fig. 2.1. Discontinuous GD basis functions,  $\phi$ , and their derivatives,  $\phi'$ , plotted for  $p=2,\ 10,\ and\ 100.$ 

contains discontinuities at element interface  $x_{j+1/2}$ , the inner product over the entire domain is decomposed into the sum of contributions over each element. Integration by parts then reveals a set of fluxes at each element boundary, which must be defined numerically. The present work focuses on wave equations in one and two space dimensions, although extension to higher dimensions is clear, and both energy conserving and dissipative upwind numerical fluxes are considered.

**3.1. Wave equation in one space dimension.** Consider first the semidiscretization of the second-order wave equation in one space dimension

$$(3.1) u_{tt} = \left(c^2 u_x\right)_x, \quad x \in \Omega,$$

where  $\Omega = [a, b]$ , and c = c(x) is a spatially dependent wave speed.<sup>1</sup> In (3.1) it will be convenient to define a flux function  $f = c^2 u_x$ . Note that in the following discussion, the treatment of physical boundary conditions is deferred until later, since it is a separate topic, and any boundary terms associated with physical boundaries are suppressed. The weak form of the PDE is derived in the usual way with multiplication by a test function  $\psi$  and integration over the domain to give

(3.2) 
$$(\psi, u_{tt})_a^b = (\psi, (c^2 u_x)_x)_a^b,$$

where  $(q, w)_{\xi}^{\eta} = \int_{\xi}^{\eta} qw \, dx$  denotes the inner product over a given interval. Expanding both the test and trial functions in the GD basis (e.g.,  $\tilde{u}(x) = \sum_{j \in \mathbf{j}} u_j \phi_j^{(p)}(x)$ , where  $j \in \mathbf{j}$  indicates the set of indices such that  $x_j \in \Omega$ ), breaking the global inner product into a sum over elements and integrating by parts over each element gives the IIPGD approximation

$$(3.3) \quad \sum_{l \in \mathbf{j}} \left( \tilde{u}_{tt}, \phi_j^{(p)} \right)_{x_{l-1/2}}^{x_{l+1/2}} = \sum_{l \in \mathbf{j}} \left\{ -\left( c^2 \tilde{u}_x, \phi_{j,x}^{(p)} \right)_{x_{l-1/2}}^{x_{l+1/2}} + \left[ f^* \phi_j^{(p)} \right]_{x_{l-1/2}}^{x_{l+1/2}^-} \right\} \quad \forall j \in \mathbf{j}.$$

In (3.3),  $[q]_{\xi}^{\eta} = q(\eta) - q(\xi)$ , and  $f^*(x_{l-1/2}) = f^*(\tilde{u}_x(x_{l-1/2}), v(x_{l-1/2}^+), v(x_{l-1/2}^-))$  is a numerical flux (to be defined) which unambiguously defines  $f = c^2 u_x$  at the element interfaces in either an energy conservative or an energy dissipative way. (The superscripts + and - denote limits from the right and left, respectively.) In the definition of the flux,  $v = u_t$  will denote the time derivative of u, i.e., the velocity. It is important to note that  $\tilde{u}_x$  has a unique definition at the element interfaces since the derivatives of the basis functions are continuous. Also note that since c is presumably a known function of x, one could compute the integrals involving c directly. Alternatively, as is done in this work, one could replace c with an interpolant  $\tilde{c}$  defined by

(3.4) 
$$\tilde{c}(x) = \sum_{j} c_j \phi_j^{(p)},$$

where  $c_j = c(x_j)$ . This approach maintains the order of accuracy of the scheme with the benefit of defining c on the domain using only the values of c at the grid points. In addition, after the interpolation of c onto the finite element space, the integrals can be computed exactly using sufficiently high-order numerical quadrature.

<sup>&</sup>lt;sup>1</sup>Smoothness assumptions on c(x) are related to assumptions of solution regularity, as required for approximation accuracy in Theorem 4.2. See Remark 1.

In order to complete the definition of the scheme, the numerical flux  $f^*$  must be defined at the element interfaces, and there are at least two natural choices. The first of these is the centered flux, in which we simply use the unambiguous definition of  $\tilde{u}_x$ , so that

(3.5) 
$$f^*(x_{l-1/2}) = c^+ c^- \tilde{u}_x(x_{l-1/2}),$$

where  $c^{\pm} = c(x_{l-1/2}^{\pm})$ . As will be shown later, this choice will lead to strict energy conservation. The second natural choice is the upwind flux, given by

(3.6) 
$$f^*(x_{l-1/2}) = c^+ c^- \tilde{u}_x(x_{l-1/2}) + \frac{c^+ c^-}{c^+ + c^-} \left[ \left[ v(x_{l-1/2}) \right] \right],$$

where  $[\![v]\!] = v^+ - v^-$  denotes the jump in the velocity. This can be derived by considering the Riemann problem for the first-order form of the acoustic wave equation with constant density

$$(3.7a) v_t - \sigma_x = 0,$$

$$\sigma_t - c^2 v_x = 0,$$

where  $\sigma = c^2 u_x$ . In the Riemann problem, denote the left states with a minus superscript, the right states with a plus superscript, and values of the solution along the interface with an I superscript. To determine the upwind flux, we must solve for the value of  $\sigma^I = c^2 u_x^I$  on the interface. The Riemann invariants of the system then imply that

(3.8a) 
$$\sigma^{I} - c^{-}v^{I} = \sigma^{-} - c^{-}v^{-},$$

(3.8b) 
$$\sigma^{I} + c^{+}v^{I} = \sigma^{+} + c^{+}v^{+},$$

since in this case the impedance in the left domain is given by  $c^-$  and the impedance in the right domain is given by  $c^+$ . Solving for  $\sigma^I$  gives the upwind flux (3.6), since in our case  $\tilde{u}_x^-(x_{l-1/2}) = \tilde{u}_x^+(x_{l-1/2}) \equiv \tilde{u}_x(x_{l-1/2})$ .

The semidiscretized system in (3.3), with upwind numerical flux (3.6), can be expressed in matrix form as

(3.9) 
$$M^{(p)}\mathbf{u}_{tt} = \left(-K^{(p)} + f_u^{(p)}\right)\mathbf{u} + f_v^{(p)}\mathbf{u}_t.$$

Here, **u** is the vector of coefficients  $u_j$ , and the mass, stiffness, and flux matrices are given by

$$\begin{split} M_{\alpha\beta}^{(p)} &= \int_{\Omega} \phi_{\alpha}^{(p)} \phi_{\beta}^{(p)} dx, \qquad K_{\alpha\beta}^{(p)} &= \int_{\Omega} \tilde{c}^2(x) \phi_{\alpha,x}^{(p)} \phi_{\beta,x}^{(p)} dx, \\ f_{u,\alpha\beta}^{(p)} &= \sum_{l \in \mathbf{j}} c^+ c^- \phi_{\beta,x}^{(p)} \phi_{\alpha}^{(p)} \big|_{x_{l-1/2}^+}^{x_{l+1/2}^-}, \qquad f_{v,\alpha\beta}^{(p)} &= \sum_{l \in \mathbf{j}} \frac{c^+ c^-}{c^+ + c^-} \left[ \left[ \phi_{\beta}^{(p)} \right] \right] \phi_{\alpha}^{(p)} \big|_{x_{l-1/2}^+}^{x_{l-1/2}^-}, \end{split}$$

where  $\alpha$  and  $\beta$  are integer indices. Specific values for the nonzero entries of the matrices are given in Table 3.1 for p = 2, and Table 3.2 for p = 4. Finally note that the scheme with the centered flux (3.5) is given by (3.9) with  $f_v^{(p)} = 0$ .

As suggested in [12, 22], the semi discrete bilinear form in (3.3) (and ultimately (3.9)) can be symmetrized. This process leads to the corresponding SIPGD method for the wave equation given as

Table 3.1

Coefficients for the interior grid points for the mass, stiffness, and flux matrices for the p=2 SIPGD scheme.

| β                         | α                  | $\alpha \pm 1$    | $\alpha \pm 2$     | $\alpha \pm 3$ |
|---------------------------|--------------------|-------------------|--------------------|----------------|
| $M_{\alpha\beta}^{(2)}$   | $\frac{143h}{160}$ | $\frac{17h}{240}$ | $\frac{-17h}{960}$ | 0              |
| $K_{\alpha\beta}^{(2)}$   | $\frac{-1}{h}$     | $\frac{1}{3h}$    | $\frac{1}{6h}$     | 0              |
| $f_{u,\alpha\beta}^{(2)}$ | $\frac{-3}{2h}$    | $\frac{1}{h}$     | $\frac{-1}{4h}$    | 0              |
| $f_{v,\alpha\beta}^{(2)}$ | $\frac{-5}{16}$    | $\frac{15}{64}$   | $\frac{-3}{32}$    | $\frac{1}{64}$ |

Table 3.2

Coefficients for the interior grid points for the mass, stiffness, and flux matrices for the p=4 SIPGD scheme.

| β                         | α                          | $\alpha \pm 1$            | $\alpha \pm 2$              | $\alpha \pm 3$         | $\alpha \pm 4$             | $\alpha \pm 5$    |
|---------------------------|----------------------------|---------------------------|-----------------------------|------------------------|----------------------------|-------------------|
| $M_{\alpha\beta}^{(4)}$   | $\frac{4160573h}{4644864}$ | $\frac{462271h}{5806080}$ | $\frac{-396211h}{11612160}$ | $\frac{5839h}{829440}$ | $\frac{-18853h}{46448640}$ | 0                 |
| $K_{\alpha\beta}^{(4)}$   | $\frac{-2605}{1728h}$      | $\frac{4969}{8640h}$      | $\frac{523}{2160h}$         | $\frac{-4079}{60480h}$ | $\frac{479}{120960h}$      | 0                 |
| $f_{u,\alpha\beta}^{(4)}$ | $\frac{-275}{256h}$        | $\frac{13}{16h}$          | $\frac{-43}{128h}$          | $\frac{1}{16h}$        | $\frac{-1}{512h}$          | 0                 |
| $f_{v,\alpha\beta}^{(4)}$ | $-\frac{567}{4096}$        | $\frac{945}{8192}$        | $\frac{-135}{2048}$         | $\frac{405}{16384}$    | $\frac{-45}{8192}$         | $\frac{9}{16384}$ |

$$\sum_{l \in \mathbf{j}} \left( \tilde{u}_{tt}, \phi_j^{(p)} \right)_{x_{l-1/2}}^{x_{l+1/2}} \\
= \sum_{l \in \mathbf{j}} \left\{ \left[ f^* \phi_j^{(p)} \right]_{x_{l-1/2}}^{x_{l+1/2}^-} + \left[ c^+ c^- \tilde{u} \phi_{j,x}^{(p)} \right]_{x_{l-1/2}}^{x_{l+1/2}^-} - \left( \tilde{c}^2 \tilde{u}_x, \phi_{j,x}^{(p)} \right)_{x_{l-1/2}}^{x_{l+1/2}} \right\} \qquad \forall j \in \mathbf{j}$$

Here  $[c^+c^-\tilde{u}\phi_{j,x}]_{x_{l-1/2}^+}^{x_{l+1/2}^-}$  is the symmetrizing term, and either the centered or the upwind numerical flux can be used to define  $f^*$ . The centered choice for  $f^*$  in (3.5) defines an energy conservative scheme, while the upwind choice of  $f^*$  in (3.6) yields an energy dissipative scheme. The SIPGD scheme has the same form as (3.9), but with  $f_u$  replaced by  $f_u + f_u^T$ .

It is important to note that typical IPG schemes for second-order operators require the addition of a penalty term of the form

(3.11) 
$$J_0(u,\phi) = \sum_{i} \frac{\sigma}{h} \llbracket u \rrbracket \llbracket \phi \rrbracket$$

with a positive lower bound on  $\sigma$ . Such a penalty term is typically needed to guarantee coercivity of the bilinear form, and therefore stability of the discretization (e.g., [22]. However, in our numerical results, and in a dispersion analysis of the discrete operators, we observe that  $\sigma = 0$  gives consistent and stable numerical approximations that converge with the expected rates. This fortuitous property is a result of the particular finite element space onto which the solution is projected. In particular, since the finite element space is the set of piecewise continuous interpolatory polynomials, the magnitude of the jumps in the solution at element faces must remain bounded and are in fact uniquely specified by the interpolation procedure. Assuming

periodicity or ignoring boundary effects, numerical experiments show that the jumps and the derivatives at the element boundaries are correlated and that the flux matrix appearing on the right-hand side of (3.10) is negative semidefinite; these are described in more detail in Appendix A. We further note that  $\sigma$  can be taken to be greater than zero and the numerical results remain essentially unchanged. In the analysis we will simply assume that  $\sigma$  has been chosen to guarantee coercivity, but we will remind the reader that in all our experiments  $\sigma=0$  has sufficed.

**3.2.** Boundary closures. As in prior GD work, the basis functions used in this work span multiple elements. As a result, near physical boundaries some modifications must be used to close the system. Various choices for boundary closures, ghost basis, extrapolation, and compatibility, have been previously discussed in [4, 5]. Nevertheless in the interest of completeness, a brief discussion of these three options as employed in this work is now provided. For a more in-depth discussion refer to [4, 5]. In the ghost basis approach, basis functions are associated with all DoFs, including at *qhost* points lying outside the physical domain, but the inner products in the weak form are taken only over the physical domain. As noted in [4], the resulting mass matrix has small values near the boundary, which can lead to poorly conditioned systems. Further, as in [5], the spectral radius of the time stepping matrix is much larger for the ghost basis approach than the other approaches, leading to a smaller time step for explicit schemes, which is also undesirable. In the current context of wave equation discretization with discontinuous basis, preliminary numerical experiments indicate that these issues may be significant, and so ghost basis closures are not considered further in this work. The other two boundary closures also employ ghost points, but the value of the solution at those points is related to the interior DoFs through algebraic formulae. Once these constraint equations are known, it is convenient to modify the basis functions so that the discretization need not contain any DoFs at ghost points. In the case of the extrapolation closure, the solution at the ghost points is obtained by pth-order extrapolation formulae. For compatibility boundary closures, the polynomial interpolants are constrained to satisfy a sequence of *compatibility* boundary conditions [4]. For example, given the wave equation with a constant wave speed, the compatibility condition for Dirichlet conditions is an odd extension of the solution across the boundary and the compatibility condition for Neumann conditions is an even extension of the solution across the boundary. Once the boundary closure has been determined, one may proceed as usual with the finite element method. Also note that for essential boundary conditions, we always modify the test and trial spaces to enforce the conditions.

**3.3.** Wave equation in two space dimensions. Consider now the variable coefficient two-dimensional (2D) wave equation,

(3.12) 
$$u_{tt} = \nabla \cdot \left(c^2(x, y)\nabla u\right), \quad (x, y) \in \Omega,$$

where here  $\Omega = [x_a, x_b] \times [y_a, y_b]$ . It will be convenient to define the flux in the x-direction as  $F = c^2 u_x$  and the flux in the y-direction as  $G = c^2 u_y$ . The corresponding weak formulation of the PDE is found by taking the inner product with a smooth test function  $\psi$  over the domain  $\Omega$  to give

<sup>&</sup>lt;sup>2</sup>Smoothness requirements on c(x, y) are again related to assumptions of solution regularity, as required for approximation accuracy in the multidimensional generalization of Theorem 4.2. See Remark 1.

(3.13) 
$$\int_{\Omega} u_{tt} \psi dA = \int_{\Omega} \psi \nabla \cdot \left( c^2(x, y) \nabla u \right) dA.$$

For the case of Cartesian geometry in two (or more) space dimensions, we seek to leverage a tensor-product formulation. Therefore, the 2D basis function is defined  $\phi_{jk}^{(p)}(x,y) = \phi_j^{(p)}(x)\phi_k^{(p)}(y)$ . Similar to one dimension, expanding both the test and trial functions in this tensor-product GD basis (e.g.,  $\tilde{u}(x) = \sum_{j \in \mathbf{j}, k \in \mathbf{k}} u_{jk} \phi_{jk}^{(p)}(x)$ , where  $j \in \mathbf{j}$  and  $k \in \mathbf{k}$  indicate the set of indices such that  $x_{jk} \in \Omega$ ), breaking the global inner product into a sum over elements, and integrating by parts over each element gives the IIPGD approximation given by

$$\sum_{l \in \mathbf{j}, m \in \mathbf{k}} \int_{\Omega} \tilde{u}_{tt} \phi_{jk}^{(p)} dA = -\sum_{l \in \mathbf{j}, m \in \mathbf{k}} \int_{\Omega} c^{2} \nabla \tilde{u} \cdot \nabla \phi_{jk}^{(p)} dA 
+ \sum_{l \in \mathbf{j}, m \in \mathbf{k}} \int_{y_{m-1/2}}^{y_{m+1/2}} \left[ F^{*} \phi_{jk}^{(p)} \right]_{x_{l-1/2}}^{x_{l+1/2}^{-}} dy 
+ \sum_{l \in \mathbf{i}, m \in \mathbf{k}} \int_{x_{l-1/2}}^{x_{l+1/2}} \left[ G^{*} \phi_{jk}^{(p)} \right]_{y_{m-1/2}}^{y_{m+1/2}^{-}} dx \qquad \forall j \in \mathbf{j}, k \in \mathbf{k},$$
(3.14)

where  $F^*$  and  $G^*$  are numerical flux functions approximating F and G, and can be either centered or upwind, as previously in one dimension. Because we have used a tensor-product basis, (3.14) can be expressed in matrix form using tensor products of 1D matrices. For example, the mass matrix  $M^{(p)}$  can be expressed  $M^{(p)} = M^{(p,x)} \otimes M^{(p,y)}$  since

$$\begin{split} M_{(\alpha\beta),(\gamma\delta)}^{(p)} &= \int_{x_a}^{x_b} \int_{y_a}^{y_b} \phi_{\alpha\beta}^{(p)}(x) \phi_{\gamma\delta}^{(p)}(y) dx dy \\ &= \int_{x_a}^{x_b} \phi_{\alpha}^{(p)}(x) \phi_{\beta}^{(p)}(x) dx \int_{y_a}^{y_b} \phi_{\gamma}^{(p)}(y) \phi_{\delta}^{(p)}(x) dy \\ &= M_{\alpha\beta}^{(p,x)} M_{\gamma\delta}^{(p,y)}. \end{split}$$

Defining  $F_u^{(p)}$ ,  $F_v^{(p)}$ ,  $G_u^{(p)}$ , and  $G_v^{(p)}$  analogously to the 1D case, we arrive at the discretization for the 2D wave equation

$$(3.15)$$

$$\left(M^{(p,x)} \otimes M^{(p,y)}\right) \mathbf{u}_{tt} = \left[\left(K^{(p,x)} + F_u^{(p)}\right) \otimes M^{(p,y)} + M^{(p,x)} \otimes \left(K^{(p,y)} + G_u^{(p)}\right)\right] \mathbf{u}$$

$$+ \left[F_v^{(p)} \otimes M^{(p,y)} + M^{(p,x)} \otimes G_v^{(p)}\right] \mathbf{u}_t.$$

This representation naturally leads to an approach to computing the solution of the system of equations by solving a number of small 1D banded matrix equations along each grid line with fixed x and y. This approach enables the solution of the system in linear time with respect to the number of grid points; see [5] for additional details. Also note that the IIPGD and SIPGD formulations both take the form of (3.15), with appropriate definitions of the matrices  $F_u$  and  $G_u$ . For variable coefficient problems in two dimensions, the matrices on the right-hand side of (3.15) lose the tensor-product structure but retain the sparsity, while the tensor-product structure of the mass matrix is retained. Therefore the cost of computing the time derivatives remains linear. Finally we note that, while not discussed in this manuscript, the literature contains

at least three approaches to geometric flexibility with GD methods. Curvilinear grids are considered in [5], block-structured grids are considered in [16], and unstructured grids are considered in [19]. One could also consider GD for overlapping grids or embedded boundaries, although these are topics for future investigation.

- 4. Analysis of the schemes. In this section, we consider various analyses of the proposed schemes. We specifically consider a 1D grid with grid spacing h (tensor-product extension to multiple dimensions is straightforward). The error analysis makes use of the results in [3, 23], although we note that the ultimate conclusions are similar to those in [12], the exception being the inclusion of the upwind flux and the properties of the GD finite element space. Therefore we first discuss the approximation properties of the GD space. Then an energy analysis of the space discretized scheme shows that the use of the upwind flux leads to energy decay while the centered flux is energy conserving. In combination, these two results show that the semidiscrete IIPGD scheme converges at the expected rate of  $\mathcal{O}(h^p)$  in the  $L_2$ -norm and the semidiscrete SIPGD scheme converges at  $\mathcal{O}(h^{p+1})$ . A dispersion relation of the discretization, which is strictly valid only for periodic or infinite domains but illustrative for parts of the domain far removed from boundaries, then illustrates a potential superconvergence at the rate  $\mathcal{O}(h^{2p})$  for the SIPGD scheme.
- **4.1. Error analysis for GD basis.** The eventual error analysis for the GD discretization of the wave equation relies on knowledge of the approximation properties of the GD basis for smooth functions. In the following,  $||\cdot||_p$  represents the  $L^p$  norm on the domain in question and  $|\cdot|_p$  represents the  $H^p$  seminorm. Note here that we always assume  $p \geq 2$ .

THEOREM 4.1 (GD error formula). Assume that the function  $u(x) \in H^{p+1}$ . Let  $\tilde{u}(x)$  be its approximation represented as an expansion in the GD basis of order p. Then there exists constant  $C_p$  independent of the grid spacing h such that

$$(4.1) ||u(x) - \tilde{u}(x)||_2 \le C_p h^{p+1} |u|_{p+1}.$$

Proof of Theorem 4.1. The use of the GD basis to represent  $\tilde{u}(x)$  is identical to considering piecewise polynomial interpolants on the dual grid. Let  $e_k$  be an element on the dual grid and let  $x \in e_k$ . Then by the error in the Lagrange interpolating polynomial, we have

(4.2) 
$$u(x) - \tilde{u}(x) = \frac{u^{p+1}(\xi)}{(p+1)!} \prod_{j} (x - x_{k+j}),$$

where j ranges over the elements over which the basis functions associated to element  $e_k$  are nonzero. Squaring and integrating over  $e_k$  and summing over the elements in the domain, we then have that

$$(4.3) ||u - \tilde{u}||_2 \le C_p h^{p+1} |u|_{p+1},$$

as desired.  $\Box$ 

Given the above approximation result, we may now demonstrate the convergence of our scheme using the arguments from [3, 12, 23], using that in general IIPG schemes converge at order p for even-order polynomial spaces and SIPG schemes converge at order p+1 for elliptic equations [22]. We explicitly assume that that the associated bilinear form is coercive. We recall that our numerical experiments show this to hold

and in any case it could be enforced, if necessary, by the addition of a penalty term. See, also, the study of the coercivity of the symbol of the method in all-space or with periodic boundary conditions presented in the appendix.

THEOREM 4.2. Suppose that the solution u(x,t) satisfies  $u, u_t \in L^{\infty}([0,T]; H^{1+s}(\Omega))$  and  $u_{tt} \in L^{\infty}([0,T]; H^s(\Omega))$  for s = p+1 and that the initial conditions u(x,0) and  $u_t(x,0)$  are set using an  $L^2$  projection onto the DGGD space. Then for any T > 0, there exists  $C_i = C_i(u,T)$  such that for the IIPGD (both centered and upwind) method

$$(4.4) ||u(\cdot,t) - \tilde{u}(\cdot,t)||_2 \le C_i h^p,$$

and a constant  $C_s = C_s(u,T)$  such that for the SIPGD (both centered and upwind) method

$$(4.5) ||u(\cdot,t) - \tilde{u}(\cdot,t)||_2 \le C_s h^{p+1}.$$

Remark 1. The assumptions on the smoothness of the solution require that the initial data satisfy  $u(x,0) \in H^{1+s}(\Omega)$ ,  $\frac{\partial u}{\partial t} \in H^s(\Omega)$  and in addition that  $c(x) \in C^s(\Omega)$ ; see, e.g., [21, Thm. 6.12].

Proof of Theorem 4.2. Note that under the regularity assumptions made, the upwind term vanishes so the error analyses are the same for both the centered and upwind schemes. The result then follows from the arguments in [3, 12, 23], provided that for  $1 \le s \le p+1$ 

(4.6) 
$$\inf_{\tilde{v} \in V^{h,p}} (||v - \tilde{v}||_2 + h||v - \tilde{v}||_{H^1}) \le h^s ||v||_s,$$

which follows from Theorem 4.1.

We note here that in practice we interpolate the initial conditions rather than performing the  $L^2$  projection, but we notice no difference in the order of accuracy of the resulting scheme. We further note that while these estimates are valid in the  $L^2$  norm, the coming grid dispersion analysis will reveal a local superconvergence in the discrete  $L^2$  norm for the SIPGD method. Additionally, the proof of Theorem 4.2 does not depend on the use of GD basis functions explicitly; the same proof holds for standard DG basis functions provided the penalty term in (3.11) is used.

**4.2. Energy estimates.** Herein we assume that the boundary conditions are periodic so that we may neglect terms associated with the boundaries. We note that numerical results to be presented later verify the stability of the scheme for non-periodic boundaries as well. Define the discrete energy by

(4.7) 
$$E_h(t) = \frac{1}{2}(u_t, u_t) + \frac{1}{2}a_h(u, u),$$

where  $a_h(u, v)$  is the bilinear form defined according to either the centered or upwind IIPGD and SIPGD schemes. We note first that the centered SIPGD bilinear form is self-adjoint, and so the scheme conserves energy, i.e.,

$$\frac{d}{dt}E_h(t) = 0.$$

Note further that the contribution of the flux terms to  $E_h$  in the IIPGD and SIPGD schemes differ only by a multiplicative constant, and so the IIPGD scheme must also satisfy (4.8). The analysis for the upwind schemes now remains the same regardless of whether the IIPGD or the SIPGD scheme is used. Without loss of generality, consider the IIPGD scheme. Upon substitution of  $u_t$  in place of  $\phi$ , we have

$$(4.9) \quad \int_{\Omega} u_{tt} u_{t} = -\int_{\Omega} c^{2} u_{x} u_{xt} + \sum_{j} \left[ c^{2} u u_{t} \right]_{x_{j-1/2}^{+}}^{x_{j+1/2}^{-}} + \sum_{j} \left[ \frac{c^{+} c^{-}}{c^{+} + c^{-}} \left[ u_{t} \right] u_{t} \right]_{x_{j-1/2}^{+}}^{x_{j+1/2}^{-}}.$$

This simplifies to

(4.10) 
$$\frac{d}{dt}E_h(t) = -\sum_{j} \left[ \frac{c^+c^-}{c^+ + c^-} \left[ u_t \right]^2 \right] \Big|_{x_{j-1/2}},$$

from which we conclude that for the upwind schemes, we have  $E'_h(t) \leq 0$  and energy dissipation. We note that (4.10) implies that for nonsmooth solutions for which the jump in the velocity is large, the dissipation in the scheme will be greater. We summarize the results of this section as the following theorem.

Theorem 4.3. The centered IIPGD and SIPGD schemes are energy conservative on a periodic domain, i.e., for the energy defined in (4.7), these schemes satisfy  $E'_h(t) = 0$ . The upwind IIPGD and SIPGD schemes are energy dissipative on a periodic domain, i.e., they satisfy  $E'_h(t) \leq 0$ .

We note here that as in the previous section, Theorem 4.3 can be proven for the standard DG basis functions as well with the inclusion of (3.11).

# 4.3. Dispersion analysis of the schemes.

**4.3.1. Analysis on a periodic domain.** The IPGD operators defined on a periodic domain with uniform grid spacing h can be analyzed using Fourier analysis since the discrete operator is translation invariant; for example, see [4]. That is to say that the discrete eigenfunctions of the operator are the discrete Fourier modes  $u_j = e^{ikx_j3}$ . Given these eigenfunctions, the symbol of the GD approximation to the second derivative is given by

(4.11) 
$$-k^2 \approx \frac{\sum_{\alpha=-p}^p (K_\alpha + f_{u,\alpha}) e^{i\eta\alpha}}{\sum_{\alpha=-p}^p M_\alpha e^{i\eta\alpha}} = \frac{1}{h^2} \mathcal{S}^{(p)}(\eta),$$

where k is a wave number and  $\eta = kh$  is a normalized grid wave number,  $M_{\alpha}$  are the coefficients in a row of the mass matrix, and  $K_{\alpha}$  are the coefficients in a row of the stiffness matrix.

Given this dispersion analysis, the accuracy of the difference operator is determined in the limit of small  $\eta$ , i.e., for small h and finite wave number k. Specifically, the local error of the approximation can be determined in this limit by considering

<sup>&</sup>lt;sup>3</sup>An alternate view of this fact is that the mass and stiffness matrices in this case are circulant and so are diagonalized with the discrete Fourier modes

the Taylor expansion of the symbol. For the IIPGD scheme with p=2,4,6,8 these expansions are

$$\begin{split} \mathcal{S}^{(2)} &= -\eta^2 + \frac{1}{8}\eta^4 - \frac{79}{2880}\eta^6 + \mathcal{O}\left(\eta^8\right), \\ \mathcal{S}^{(4)} &= -\eta^2 + \frac{3}{128}\eta^6 - \frac{5}{1024}\eta^8 + \mathcal{O}\left(\eta^{10}\right), \\ \mathcal{S}^{(6)} &= -\eta^2 + \frac{5}{1024}\eta^8 - \frac{35}{24576}\eta^{10} + \mathcal{O}\left(\eta^{12}\right), \\ \mathcal{S}^{(8)} &= -\eta^2 + \frac{35}{32768}\eta^{10} - \frac{105}{262144}\eta^{12} + \mathcal{O}\left(\eta^{14}\right). \end{split}$$

Clearly the error in the symbol is  $\mathcal{O}(h^p)$ , in agreement with Theorem 4.2, and in similarity with analysis of other IIPG schemes [22]. Note also that all terms in the expansion are of even order and real, which implies that the spatial errors in the eventual wave solver are purely dispersive, i.e., there will be no dissipation for these centered difference schemes.

Similar analyses can be applied to the derivative approximation implied by the symmetric interior penalty method to give

$$\begin{split} \mathcal{S}^{(2)} &= -\eta^2 - \frac{19}{2880} \eta^6 + \frac{79}{40320} \eta^8 + \mathcal{O}\left(\eta^{10}\right), \\ \mathcal{S}^{(4)} &= -\eta^2 - \frac{93937}{232243200} \eta^{10} + \frac{234049}{1532805120} \eta^{12} + \mathcal{O}\left(\eta^{14}\right), \\ \mathcal{S}^{(6)} &= -\eta^2 - \frac{13968274213}{669529276416000} \eta^{14} + \frac{6167441597}{573882236928000} \eta^{16} + \mathcal{O}\left(\eta^{18}\right), \\ \mathcal{S}^{(8)} &= -\eta^2 - \frac{7605288411403}{6993099386309836800} \eta^{18} + \frac{2804978478591101}{3875342576580034560000} \eta^{20} + \mathcal{O}\left(\eta^{22}\right). \end{split}$$

Hence, the local dispersion analysis demonstrates that the SIPGD derivative approximation exhibits superconvergence at the grid points with order  $\mathcal{O}(h^{2p})$ . Remarkably, this is the same superconvergence rate observed for the GD scheme with continuous basis as discussed in [4].

In order to analyze the effects of the upwind flux, we must consider the full semidiscretization of the wave equation, (3.9). Taking the Laplace transform in time, and assuming Fourier mode spatial eigenfunctions, we arrive at the equation

(4.12) 
$$\left( s^2 \sum_{\alpha} M_{\alpha} e^{ikh\alpha} - s \sum_{\alpha} F_{v,\alpha} e^{ikh\alpha} - (K_{\alpha} + F_{u,\alpha}) e^{ikh\alpha} \right) \hat{u} = 0,$$

where s is the dual Laplace variable, k is the wave number, and  $\hat{u}$  is used to indicate the transformed quantities. The dispersion relation for the continuous wave equation implies that  $s \approx \pm ik$ , and the discrepancy between this continuous result and solutions to (4.12) for finite k number and small h reveal the accuracy of the scheme. For the upwind IIPGD scheme with p = 2, Equation (4.12) gives that

$$(4.13) s = ik \left( 1 - \frac{1}{16} \eta^2 + \frac{271}{23040} \eta^4 - \frac{5503}{2580480} \eta^6 + \frac{2582861}{7431782400} \eta^8 + \mathcal{O}(\eta^{10}) + \frac{i}{128} \eta^5 - \frac{i}{512} \eta^7 + \mathcal{O}(\eta^9) \right)$$

and its complex conjugate. Clearly the error in this dispersion relation indicates  $\mathcal{O}(h^2)$  accuracy, as expected. Furthermore, the arrangement of (4.13) is intended to

facilitate a deeper understanding of the behavior of the scheme. In particular, the first line of (4.13) proceeds in even powers of  $\eta$  and indicates pure dispersion errors. The second line, however, proceeds in odd powers of  $\eta$  and represents dissipation terms which have entered due to the use of the upwind flux. It is particularly important to notice that the dissipation errors in (4.13) enter at  $\mathcal{O}(h^5)$ , while the dispersion errors enter at  $\mathcal{O}(h^2)$ . This order separation between the dispersion and dissipation errors indicates that although the upwind IIPGD scheme is dissipative, the scheme may appear to have limited dissipation for all but the very highest frequency modes. Similarly for the upwind IIPGD scheme with p = 4, (4.12) gives

(4.14) 
$$s = ik \left( 1 - \frac{3}{256} \eta^4 + \mathcal{O}(\eta^6) + \frac{9i}{32768} \eta^9 + \mathcal{O}(\eta^{11}) \right)$$

and its complex conjugate. Thus the method is  $\mathcal{O}(h^4)$ , but the effects of upwind dissipation do not enter until  $\mathcal{O}(h^9)$ . This general trend continues as p is increased, and the upwind IIPGD schemes have accuracy  $\mathcal{O}(h^p)$ , with the dissipation error entering at  $\mathcal{O}(h^{2p+1})$ .

On the other hand, the dispersion analysis of the upwind SIPGD scheme with p=2 yields

(4.15) 
$$s = ik \left( 1 + \frac{19}{5760} \eta^4 - \frac{79}{80640} \eta^6 + \frac{9323}{66355200} \eta^8 + \mathcal{O}(\eta^{10}) + \frac{i}{128} \eta^5 - \frac{i}{512} \eta^7 + \mathcal{O}(\eta^9) \right)$$

and its complex conjugate. Not only does (4.15) reveal a nodal superconvergence as  $\mathcal{O}(h^4)$ , the effects of the upwind dissipation enter at  $\mathcal{O}(h^5)$ ), just one order higher than the leading dispersion error. Similarly the upwind SIPGD scheme with p=4 has

$$(4.16) s = ik \left( 1 + \frac{93937}{464486400} \eta^8 + \mathcal{O}(\eta^{10}) + \frac{9i}{32768} \eta^9 + \mathcal{O}(\eta^{11}) \right)$$

and its complex conjugate. Again, the nodal superconvergence is revealed, and as for p=2, the effects of dissipation enter at only one order higher than the leading dispersion error. This trend continues and the upwind SIPGD schemes have accuracy  $\mathcal{O}(h^{2p})$ , with the dissipation error entering at  $\mathcal{O}(h^{2p+1})$ . The fact that the dissipation error in the SIPGD schemes is only one order higher than the leading dispersion error, while for the IIPGD schemes the separation is p/2, is expected to have a significant impact on the behavior of numerical approximations. This difference will be investigated numerically in section 5.

**4.3.2.** Discrete analysis on a bounded domain. In section 4.3.1, a dispersion analysis was used to investigate the properties of the IIPGD and SIPGD schemes for a periodic domain. It is also useful to perform an analysis on a bounded domain so that the effects of boundary closures can be taken into account. An analytic investigation of the spectrum with boundaries is beyond the scope of the present work, and so instead we choose to present the discrete spectra of the spatial operator for the various schemes for a particular problem. To that end, we first convert (3.9) into a first-order temporal system as

$$\begin{bmatrix} \mathbf{u} \\ \mathbf{v} \end{bmatrix}_t = \begin{bmatrix} 0 & I \\ M^{-1} \left( K + F_u \right) & M^{-1} F_v \end{bmatrix} \begin{bmatrix} \mathbf{u} \\ \mathbf{v} \end{bmatrix}.$$

The discrete equations are treated as a single large system of equations  $\mathbf{w}_t = \mathbf{D}\mathbf{w}$ , where  $\mathbf{w} = [\mathbf{u}, \mathbf{v}]^T$ , and the discretization matrix  $\mathbf{D}$  is defined as

$$\mathbf{D} = \begin{bmatrix} 0 & I \\ M^{-1} \left( K + F_u \right) & M^{-1} F_v \end{bmatrix}.$$

Figure 4.1 shows the eigenvalues of the  ${\bf D}$  matrix for different orders and boundary closures for p=2 and p=8 on the domain  $\Omega=[-1,1]$ , using a grid with N=21 grid points, Dirichlet boundary conditions, and constant wave speed c=1. Note that for higher-order methods, the spectral radius of the operator increases, but this increase is mild. This implies that the time step restriction for explicit schemes is relatively lax. We observe that the eigenvalues for the centered scheme all lie on the imaginary axis, which implies that modes oscillate but do not grow or decay in time, in agreement with both the energy estimates of section 4.1 and the Fourier analysis of section 4.3.1. In contrast, the upwind flux pushes the eigenvalues into the left half-plane leading to time decay. Note that high-frequency modes are observed to decay faster than low-frequency modes, again in agreement with the dispersion relation determined by the Fourier analysis. Similarly, Figure 4.2 shows the eigenvalues of the same operator for the SIPGD scheme. The spectrum of both the compatibility and extrapolation boundary conditions have very similar behavior as for the IIPGD case.

5. Numerical results. In this section, numerical results are presented which verify the convergence and stability properties discussed in the prior sections. Additional results for solutions lacking sufficient regularity to ensure high orders of convergence, for example, solutions with discontinuities, are also presented in order to demonstrate the favorable properties of the upwind schemes, and in particular the

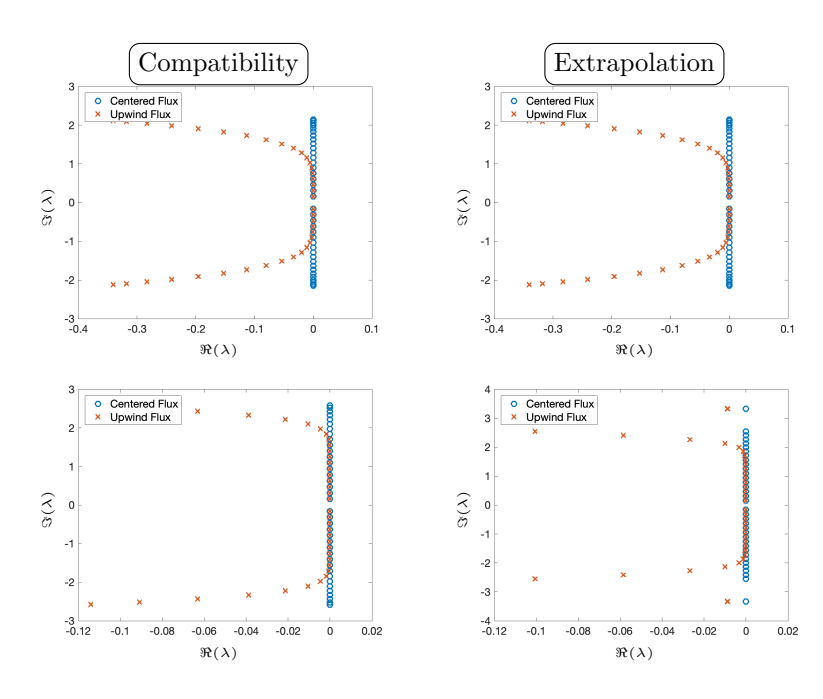


FIG. 4.1. Location of the eigenvalues in the complex plane for the IIPGD discretization operators with the centered (blue circle) and upwind (red x) fluxes with N=21 points in the domain. The top row corresponds to p=2, the bottom row corresponds to p=8, and the columns correspond to the compatibility and extrapolation boundary closures, respectively.

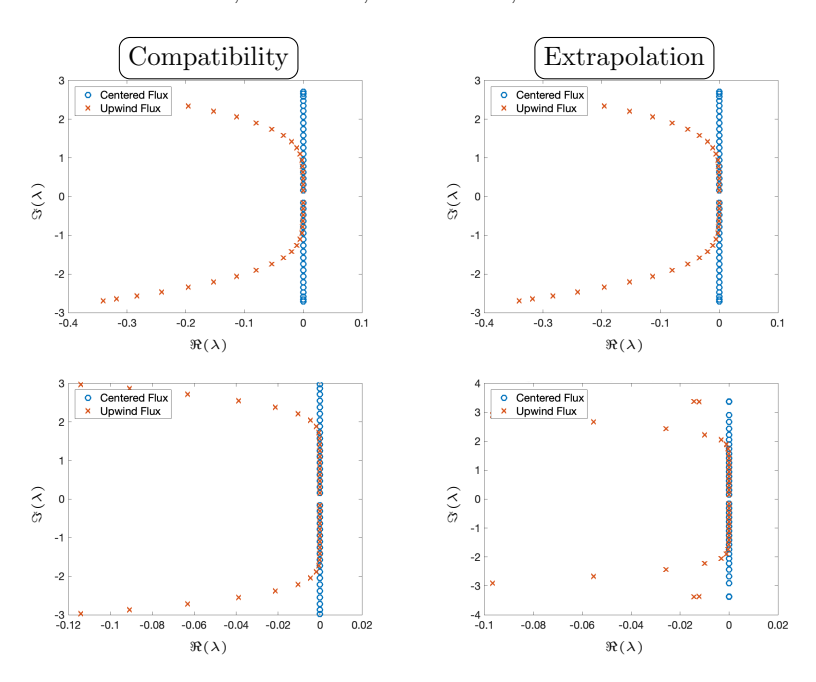


Fig. 4.2. Location of the eigenvalues in the complex plane for the SIPGD discretization operators with the centered (blue circle) and upwind (red x) fluxes with N=21 points in the domain. The top row corresponds to p=2, the bottom row corresponds to p=8, and the columns correspond to the compatibility and extrapolation boundary closures, respectively.

symmetrized SIPGD discretization. For all results except the cylinder scattering problem, time is discretized using a Taylor time stepper of order p+2 for the IIPGD scheme and 2p+2 for the SIPGD scheme so that the observed convergence is that of the spatial discretization. Given the semidiscretization  $u_{tt} = D_h u$ , the precise form of the time stepping scheme is

(5.1) 
$$u(t + \Delta t) = \sum_{j=0}^{s} \frac{(\Delta t)^{j}}{j!} D_{h}^{j} u(t),$$

where s is the order of the method. This section proceeds by first considering 1D results in section 5.1, followed by 2D results in section 5.2.

## 5.1. One-dimensional results.

**5.1.1.** Convergence for constant coefficients. Consider first the computation of a standing wave solution to the wave equation with constant wave speed in one space dimension. Without loss of generality, take c=1 and take the domain to be  $\Omega=[0,.5]$ . Let the boundary condition at x=0 be a homogeneous Dirichlet condition and the boundary condition at x=0 be a homogeneous Neumann condition. An exact standing wave solution is given by  $u(x,t)=\cos(k\pi t)\sin(k\pi x)$ , for k an integer chosen so that the solution satisfies the boundary conditions. For the computational results presented in Figure 5.1, we take k=25 and run to a final time of  $t_f=1.45$ . We also note that  $L_h^2$  denotes the discrete  $L^2$  norm computed at the grid points, computed by  $||u||_{L_h^2}=\sqrt{\frac{1}{\Delta x}\sum_{j\in \mathbf{j}}u_j^2}$ , while  $L^2$  specifies the true  $L^2$  norm (computed using Gauss quadrature to order p+2 so that the accuracy observed is that of the scheme).

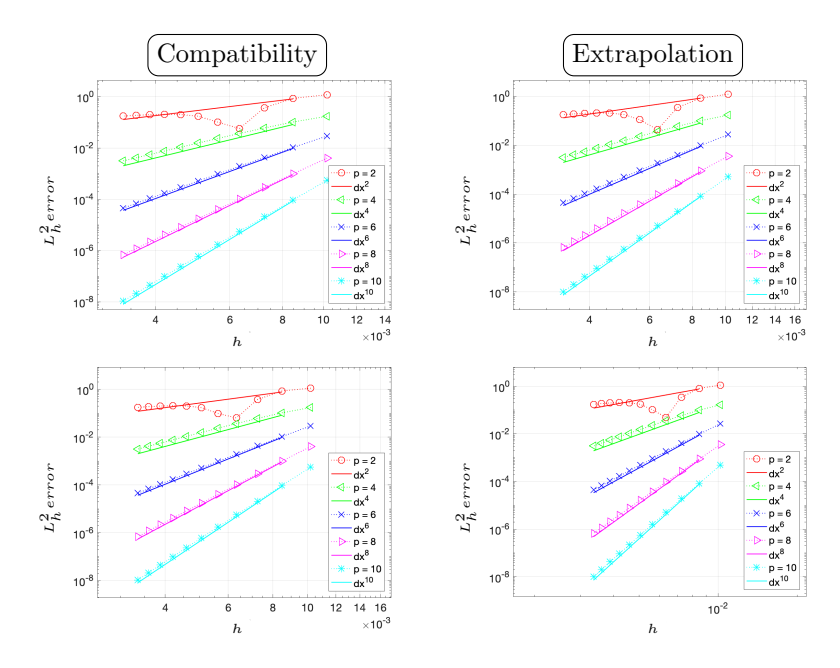


Fig. 5.1. Convergence results of the IIPGD scheme for a standing wave. The first row shows results for the centered flux, while the bottom row shows results for the upwind flux. The observed  $L_h^2$  error in each computation is plotted using marks, while solid lines are references corresponding to order  $h^p$  convergence.

The same case is repeated for the SIPGD scheme. Here, we present only the results using the compatibility boundary conditions, since this is the only case which exhibits the superconvergence predicted by the grid dispersion analysis. Figure 5.2 presents the errors and convergence rates with both the discrete and true  $L^2$  norms. With the use of compatibility conditions, the super convergence predicted from the local dispersion analysis is observed in the discrete  $L^2$  norm. The expected convergence rate in the true  $L^2$  norm determined by the approximation results are also observed.

Next, extrapolation boundary conditions are tested in conjunction with the SIPGD scheme in Figure 5.3. The purpose of this test is to reveal the dominance of the dispersion error for domains which are sufficiently large in space or time. Thus a final time of  $t_f = 25.4$  is used, and we take k = 61. For lower-order methods at the resolutions tested, superconvergence at order  $\mathcal{O}(h^{2p})$  is demonstrated. For higher-order methods, the scheme converges at order  $\mathcal{O}(h^{2p})$  for coarse grids, while approaching order  $\mathcal{O}(h^{p+1})$  on finer grids. It is expected that superconvergence would be observed on finer grids for longer final times or larger domains. This is consistent with the results for the corresponding continuous basis functions presented in [4].

In order to more clearly understand the superconvergence observed in the SIPGD scheme, it is instructive to look more closely at the spatial error in approximations for this case of constant wave speed. Figures 5.4 and 5.5 show the errors in the IIPGD and SIPGD schemes respectively for a standing wave with a single period on the domain  $\Omega = [0,1]$  using compatibility boundary conditions. The scheme is advanced to a final time of  $t_f = .45$  and the error is plotted over each element. As is common for finite difference methods, the error at the grid points is smooth and, in this case, essentially sinusoidal. Additionally, the error for the SIPGD scheme clearly shows the effects of the superconvergence on the error since the grid points are near the locations where the error in the approximation changes sign.

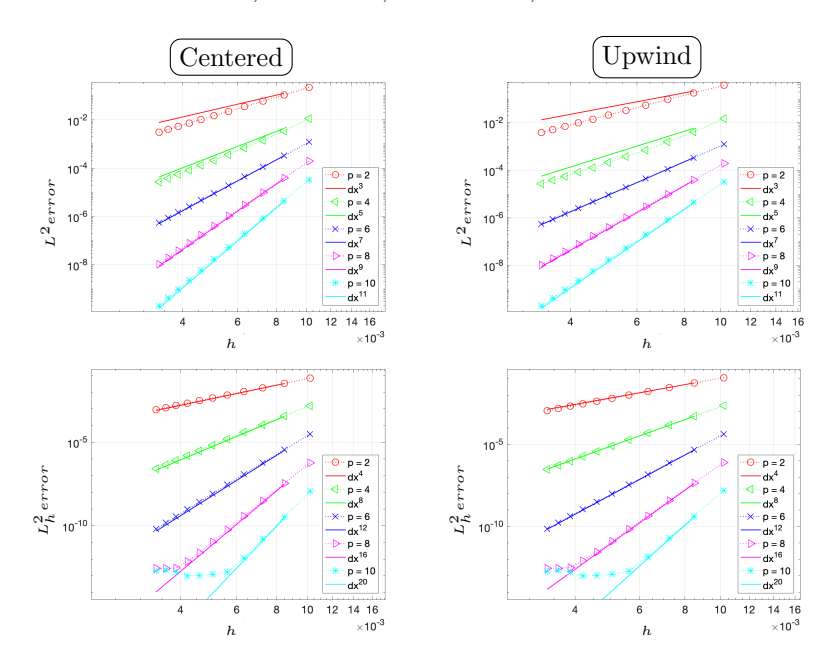


FIG. 5.2. Convergence results of the SIPGD scheme for a standing wave solution using the compatibility boundary closure. The first row shows the true  $L^2$  norm and the second row shows the discrete  $L_h^2$  norm, while the first column shows the results for the centered scheme and the second shows the results for the upwind scheme. The SIPGD converges at the expected  $\mathcal{O}(h^{p+1})$  and  $\mathcal{O}(h^{2p})$  rates in the true and discrete  $L^2$  norms, respectively.

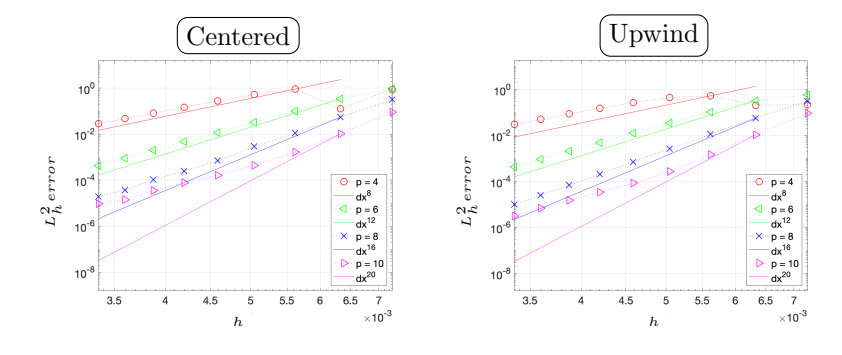


Fig. 5.3. Convergence results of the SIPGD scheme for a standing wave solution using the extrapolation boundary closure. For smaller p we observe superconvergence, while for larger p we observe a transition from the superconvergent  $\mathcal{O}(h^{2p})$  to the expected asymptotic rate of  $\mathcal{O}(h^{p+1})$ .

**5.1.2.** Performance for singular solutions. To illustrate the effect of numerical upwinding, we now consider a series of tests for solutions with singular behavior. In particular, consider two sets of initial conditions that lead to nonclassical weak solutions of the wave equation:

(5.2) 
$$u_0(x) = \begin{cases} \frac{x - x_l}{x_m - x_l}, & x_l < x < x_m, \\ \frac{x_r - x}{x_r - x_m}, & x_m < x < x_r, \\ 0 & \text{otherwise,} \end{cases}$$

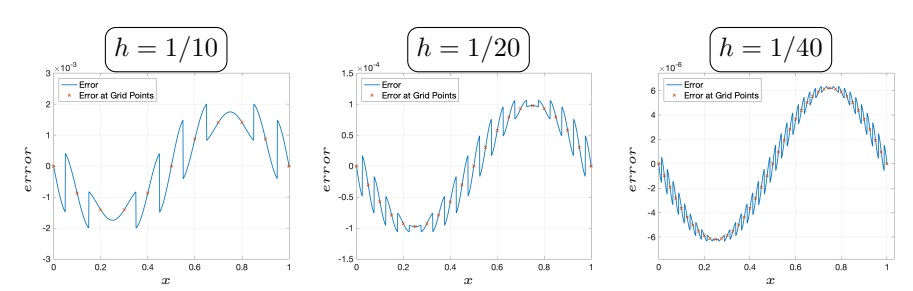


Fig. 5.4. Plots of the error for the standing wave solution with one period at t = .45 at different grid resolutions for p = 4 with the upwind IIPGD scheme with compatibility conditions. Only results for the upwind method are shown since results for the centered scheme are virtually identical.

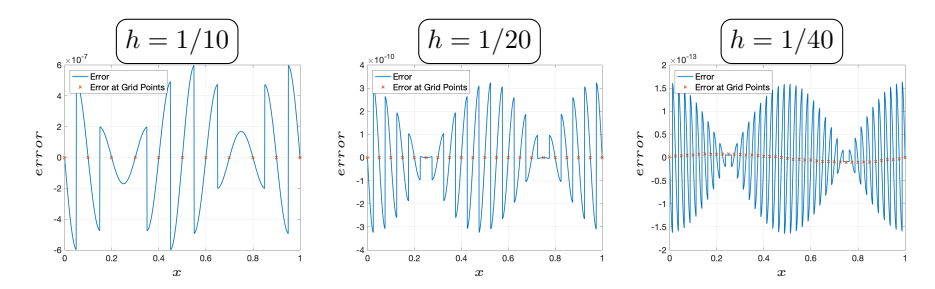


Fig. 5.5. Plots of the error for the standing wave solution with one period at t=.45 at different grid resolutions for p=4 with the upwind SIPGD scheme with compatibility conditions. Only results for the upwind method are shown since results for the centered scheme are virtually identical.

and

(5.3) 
$$u_0(x) = \begin{cases} 1, & x_l < x < x_r, \\ 0 & \text{otherwise,} \end{cases}$$

with the initial velocity in both cases being set to zero. In both cases, exact formal solutions can be determined using the D'Alembert solution. Figure 5.6 shows the computed displacement u and velocity v at t=.7 for initial conditions (5.2) computed using schemes corresponding to p=2 and p=10. Results for the centered IIPGD scheme, the upwind IIPGD scheme, and the upwind SIPGD scheme are included. The effects of the upwinding is clear, with high-frequency numerical oscillations originating from the discontinuity in velocity being damped by the dissipation inherent to the upwind flux. In addition, the effect of the order separation between dispersive and dissipative errors for the upwind SIPGD scheme, versus the more closely ordered dispersive and dissipative errors for the upwind SIPGD scheme, are apparent, with the SIPGD scheme yielding qualitatively superior results.

To further investigate this distinction between upwind IIPGD and SIPGD schemes, Figure 5.7 shows results for the initial conditions given in (5.3). Here the solution is rather weak and contains discontinuities in u and delta functions in v. Nevertheless the schemes are seen to be remarkably effective, and again the effect of upwinding is clear, and high-frequency numerical oscillations in both u and v are effectively damped by the dissipative error. Since the upwind SIPGD scheme with p=2 is formally fourth-order accurate for smooth solutions, and we might expect the discontinuities to be better resolved than for either of the other schemes with p=2.

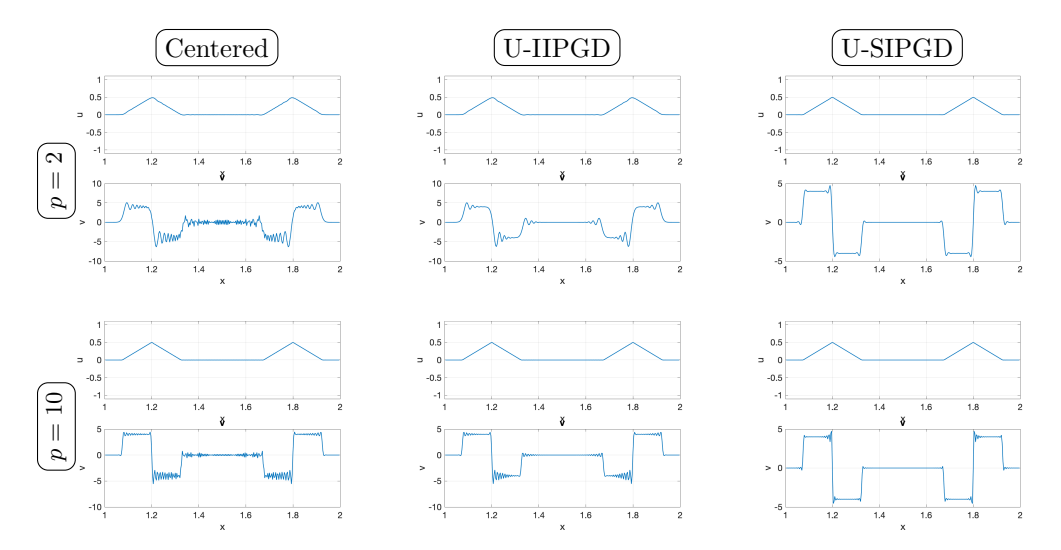


Fig. 5.6. Plots of the computed solution to the wave equation for the initial condition given in (5.2) computed with N=300 grid points. The first row is for p=2 and the second row is for p=10. The first column is the centered IIPGD scheme, the second column is the upwind IIPGD scheme, and the final column is the upwind SIPGD scheme.

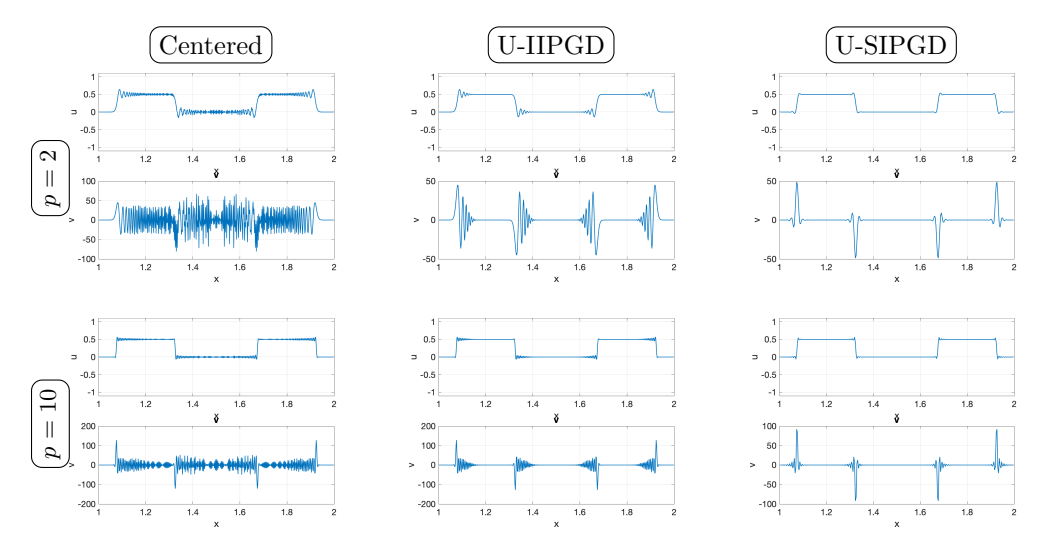


Fig. 5.7. Plots of the computed solution to the wave equation for the initial condition given in (5.3) computed with N=300 grid points. The first row is for p=2 and the second row is for p=10. The first column is the centered IIPGD scheme, the second column is the upwind IIPGD scheme, and the final column is the upwind SIPGD scheme.

This is born out by the results. Further, one could argue that the results for the upwind SIPGD scheme with p=2 are qualitatively better than the results for the other schemes with p=10.

**5.1.3.** Convergence for variable coefficients. Consider now the 1D variable coefficient equation. To facilitate quantitative convergence studies, it is useful to derive an exact solution. To that end we pose a time harmonic solution of the form

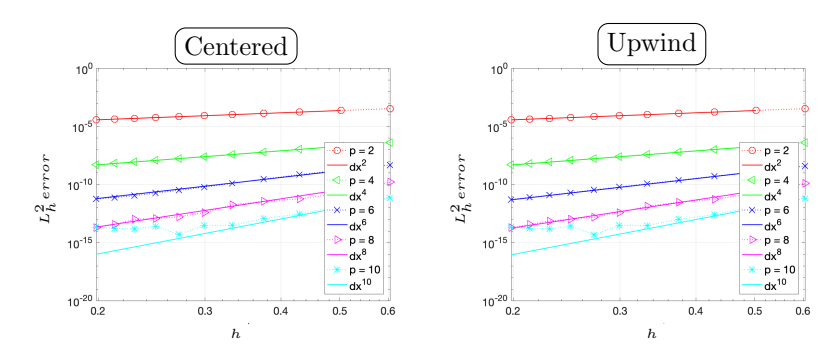


Fig. 5.8. Convergence results for the IIPGD scheme with exact solution determined in (5.5). The first column shows the results for the centered flux and the second column shows the results for the upwind flux.

 $u(x,t) = \cos(\omega t)\psi(x)$ , and so  $\psi(x)$  must satisfy

$$(5.4) -\omega^2 \psi(x) - 2c(x)c'(x)\psi'(x) - c^2(x)\psi''(x) = 0.$$

To specify a solution, we take  $c(x) = 2\sqrt{x}$ , and  $\omega = 1$ , so that the solution to (5.4) is

(5.5) 
$$u(x,t) = \cos(t) \left( J_0(\sqrt{x}) + Y_0(\sqrt{x}) \right).$$

Here  $J_0$  and  $Y_0$  are, as usual, Bessel functions of the first and second kind, respectively. The domain for the computation is chosen as [a, b] = [10.1078784750822, 39.7249819922633], and homogeneous Dirichlet boundary conditions are used. The computation is run to a final time of  $t_f = 1.45$ . Results of a convergence study using this exact solution are shown in Figure 5.8. Here the IIPGD scheme is used, extrapolation boundary conditions are applied, and results are presented for both centered and upwind numerical fluxes. Note that we do not include results for the scheme with compatibility closures since the derivation of the scheme for the variable coefficient problem is not straightforward, and has therefore not been pursued here.

### 5.2. Two-dimensional results.

**5.2.1. Convergence for constant coefficients.** Consider now the constant coefficient case with c=1 in two space dimensions. For purposes of illustrating convergence behavior, we take the exact solution as

(5.6) 
$$u(x, y, t) = \cos(\sqrt{2\pi kt})\sin(k\pi x)\sin(k\pi y).$$

In order to test the efficacy of the scheme with a variety of boundary conditions, we take the domain to be  $[0, 1.25] \times [0, 1.25]$  and apply homogeneous Dirichlet conditions on the bottom and left boundaries and homogeneous Neumann conditions on the top and right boundaries. The computation is run to a final time of  $t_f = 5.4$  with k = 6. Figure 5.9 shows the results of the HPGD scheme applied to this problem setup with  $h = \Delta x = \Delta y$  and using both extrapolation and compatibility boundary closures. The expected convergence rate  $\mathcal{O}(h^p)$  is observed in each case.

To illustrate the superconvergent behavior of the SIPGD scheme in two space dimensions, Figure 5.10 shows results of convergence studies using the SIPGD scheme with extrapolation boundary conditions. Here, the standing wave solution (5.6) with k = 10 is used, the final time is taken to be  $t_f = 25.4$ , and the grid is again chosen with  $\Delta x = \Delta y = h$ . As in the 1D case, the lower-order methods exhibit superconvergence across the whole range of grid resolutions, while high-order schemes exhibit

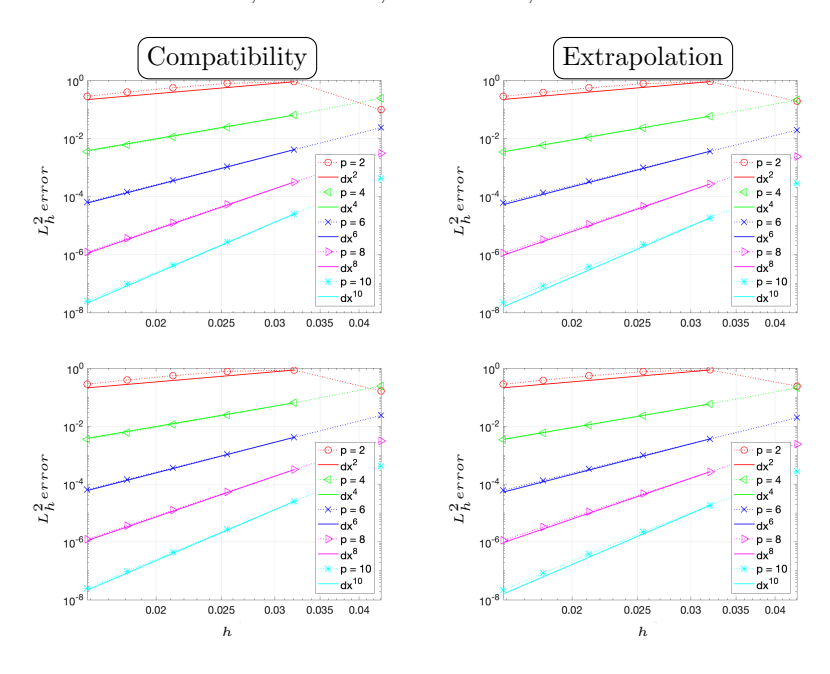


Fig. 5.9. Results for the convergence study using the 2D IIPGD schemes with constant coefficients and a standing wave solution. As expected, convergence at  $\mathcal{O}(h^p)$  is observed in all cases.

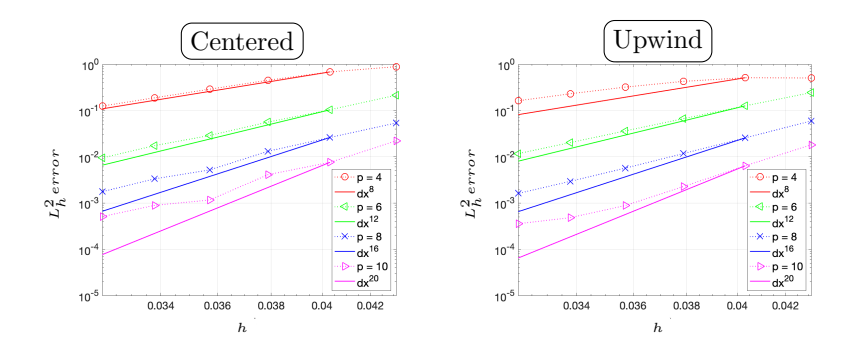


Fig. 5.10. Results for convergence studies for the standing wave solution (5.6) with k = 10 and  $t_f = 25.4$ . Here the SIPGD scheme is used, and extrapolation boundary closures are applied. For low p, superconvergence is observed for all resolutions, while for larger p the initial superconvergence gives way to the asymptotic  $\mathcal{O}(h^{p+1})$  rate.

superconvergence for coarse grids but transition to the asymptotic  $\mathcal{O}(h^{p+1})$  for finer grids. Note that had compatibility conditions been used, the SIPGD scheme would exhibit superconvergence for all grid resolutions.

**5.2.2.** Convergence for variable coefficients. Next, we consider the 2D variable coefficient equations for the domain  $[0,1] \times [0,1]$  with homogeneous Dirichlet conditions on all boundaries. An exact solution can, in principle, be derived using techniques similar to the 1D case, but we instead choose to employ the method of manufactured solutions. Therefore, consider the forced wave equation

$$(5.7) u_{tt} = \nabla \cdot (c^2 \nabla u) + f$$

with f defined so that the manufactured solution is

(5.8) 
$$u(x, y, t) = \beta(t+1)(x - x_a)^{\kappa}(x - x_b)^{\kappa}(y - y_a)^{\kappa}(y - y_b)^{\kappa}.$$

Here  $\kappa=10$  is chosen so that the solution and its derivatives are zero at the boundary to sufficient order,  $\beta=1e12$  is chosen so that the solution is order one at the final time  $t_f=5.4$ , and the wave speed is taken to be

(5.9) 
$$c(x,y) = \sin(xy) + \frac{3}{2}.$$

Results for a series of convergence studies using the IIPGD scheme are shown in Figure 5.11. The expected asymptotic convergence rate of  $\mathcal{O}(h^p)$  is observed for all cases as the grid is refined. Note that as in one dimension, results for the scheme with compatibility boundary closures are omitted due to the difficulty of deriving them for variable wave speed.

**5.2.3.** Scattering from a circular cylinder. As a further test involving variable coefficients, a curvilinear coordinate mapping is introduced in order to address scattering of a plane wave by a unit cylinder. Precisely, consider the time-periodic solution of the scalar wave equation in cylindrical coordinates in the domain  $(r,\theta) \in (1,\infty) \times (0,2\pi)$  for 0 < t < 20. The incident wave is taken as

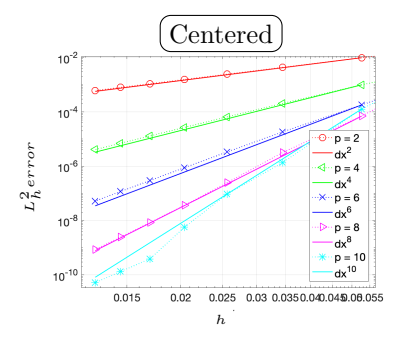
$$(5.10) u_{\rm inc} = \cos\left(k(x - ct)\right)$$

with k = 100 defining the spatial frequency, and the wave speed is set as c = 1. As is common in exterior problems, the solver is used to approximate the scattered field whose governing equations are

$$\frac{\partial^2 u}{\partial t^2} = c^2 \left( \frac{1}{r} \frac{\partial}{\partial r} \left( r \frac{\partial u}{\partial r} \right) + \frac{1}{r^2} \frac{\partial^2 u}{\partial \theta^2} \right).$$

At the cylinder surface, the standard boundary condition for the scattered field is

(5.11) 
$$\frac{\partial u}{\partial r}(1,\theta,t) = -\frac{\partial u_{\text{inc}}}{\partial r}(1,\theta,t) \equiv g_1(\theta,t).$$



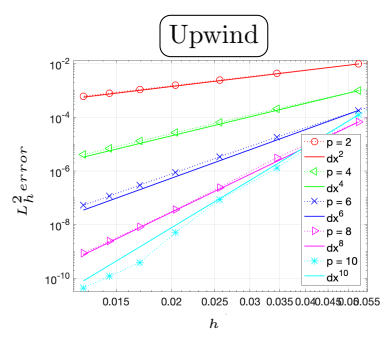


Fig. 5.11. Results of convergence studies for the IIPGD schemes for the 2D equations with variable coefficients. Manufactured solutions with the exact solution corresponding to (5.8) are used.

An exact expression for the scattered field is (see, e.g., [20, Chap. 4.2])

$$(5.12) \ u_{\rm sc} = -\Re\left(e^{-kict}\left(\frac{J_0'(k)}{H_0^{(1)'}(k)}H_0^{(1)}(kr) + 2\sum_{\ell=1}^{\infty}i^{\ell}\frac{J_\ell'(k)}{H_\ell^{(1)'}(k)}H_\ell^{(1)}(kr)\cos\left(\ell\theta\right)\right)\right),$$

where  $J_{\ell}$  and  $H_{\ell}^{(1)}$  are Bessel and Hankel functions of the first kind, respectively. In the computations, the sum is truncated to  $\ell \leq 250$ , which experiments show exceeds what is necessary to deliver 15-digit accuracy in the presented cases.<sup>4</sup>

Computations are performed on the domain  $(r, \theta) \in (1, 2) \times (0, 2\pi)$ , where the boundary at r = 2 is an artificial truncation of the infinite domain. At this radiation boundary a low-order radiation boundary condition is applied, with inhomogeneous forcing so that (5.12) remains the exact solution:

(5.13) 
$$\frac{\partial u}{\partial t}(2,\theta,t) + c\frac{\partial u}{\partial r}(2,\theta,t) + \frac{c}{4}u(2,\theta,t)$$
$$= \frac{\partial u_{\rm sc}}{\partial t}(2,\theta,t) + c\frac{\partial u_{\rm sc}}{\partial r}(2,\theta,t) + \frac{c}{4}u_{\rm sc}(2,\theta,t) \equiv g_2(\theta,t).$$

Note that we could also have simply imposed exact Dirichlet or Neumann data at r=2 but chose to illustrate the discretization of a prototypical boundary operator used for scattering problems. Initial conditions,  $u_{\rm sc}(r,\theta,0)$  and  $\frac{\partial u_{\rm sc}}{\partial t}(r,\theta,0)$ , follow directly from (5.12).

The numerical experiments presented below use the SIPDG method with the upwind flux, polynomials of degree p=8, and extrapolation boundary closures at r=1 and r=2. Given the simple time-dependence of the inhomogeneous data, Taylor time stepping could have been used, but it is more typical to employ Runge–Kutta methods. Therefore in contrast with the other examples in this manuscript, the standard fourth-order four-stage Runge–Kutta method was used for time stepping. The SIPDG method takes a simple form in this case due to the orthogonality of the coordinate system. In particular the semidiscrete system can be expressed in tensor-product form as

$$M_r \otimes M_\theta \mathbf{u}_{tt} = ((-K_r + f_{u,r}) \otimes M_\theta + D_r \otimes (-K_\theta + f_{u,\theta})) \mathbf{u}$$
  
 
$$+ (f_{v,r} \otimes M_\theta + M_r \otimes f_{v,\theta}) \mathbf{u}_t - E_1 \otimes M_\theta g_1 + E_2 \otimes M_\theta \left( \mathbf{u}_t + \frac{c}{4} \mathbf{u} - g_2 \right).$$

Here the radial integrals are properly weighted by the Jacobian r,  $D_r$  arises from the Galerkin representation of multiplication by  $r^{-2}$ , and the boundary terms arise from replacing  $\frac{\partial u}{\partial r}$  arising from the construction of  $K_r$  by the boundary conditions (5.11)–(5.13). Note that the functions  $g_{1,2}(\theta,t)$  are the inhomogeneities defined in (5.11) and (5.13), respectively, and the matrices  $E_{1,2}$  evaluate the basis functions at the boundaries. Given the tensor-product form, the computation of  $\mathbf{u}_{tt}$  remains linear in the number of grid points.

Simulation results are presented in Figure 5.12, which shows the computed scattered field and solution error at t=10 from a simulation using 300 points in the radial direction, 900 points in the azimuthal direction, and 100000 time steps for  $t \in (0, 10]$ . The spatial resolution corresponds to roughly 9 points-per-wavelength, and the time step has been taken intentionally small so that spatial errors dominate. Clearly the

 $<sup>^4</sup>$ Note that for the cases presented the max-norm of the first neglected term in the sum in (5.12) is approximately  $10^{-73}$ , indicating that the truncated sum is exact within the confines of double precision arithmetic.

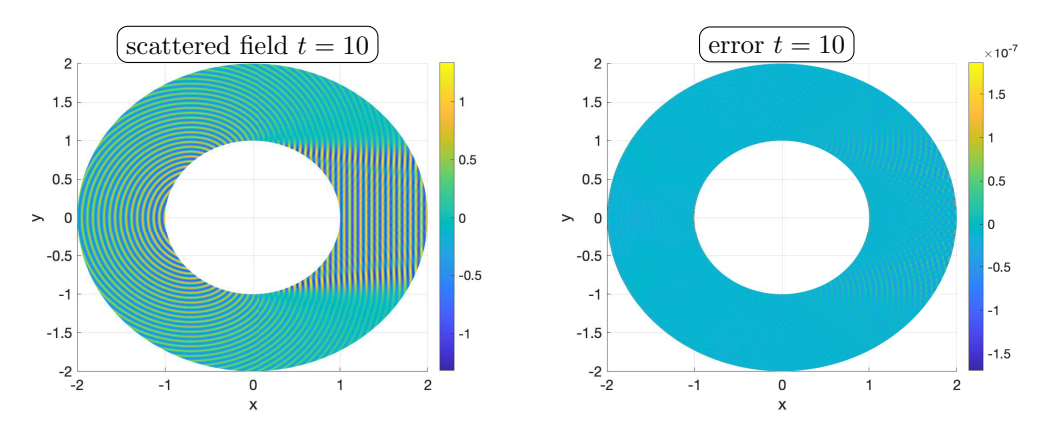


Fig. 5.12. Computed scattered field (left) and solution error (right) at t = 10 from a simulation using 300 points in the radial direction, 900 points in the azimuthal direction, and 100000 time steps for  $t \in (0, 10]$ .

boundary errors are beginning to dominate the errors on the domain interior, although in coarser runs the interior error is more comparable to the boundary error. As has been seen previously, this behavior is typical of the symmetric GD discretizations where superconvergence at  $\mathcal{O}(h^{2p})$  is often observed for coarse grids, but for fine grids the expected rate transitions to  $\mathcal{O}(h^{p+1})$ . This behavior can clearly be observed by considering a grid refinement study, as presented in Figure 5.13. The details of the grid and time steps are indicated in the table, but in terms of the wavelength of the incident wave these grids correspond to roughly 4.5, 6, 9, and 12 points-per-wavelength. The time step is aggressively refined to match the higher-order accuracy of the spatial discretizations. To reflect the temporal evolution of the error, the convergence study uses the relative discrete  $L_h^2$  norm in the full space-time domain with  $t \in (0, 20]$ . Early in the refinement process the convergence rates are higher than the expected order  $\mathcal{O}(h^{p+1})$  and likely are approaching the superconvergent rate of  $\mathcal{O}(h^{2p})$ . However, as the boundary errors come to dominate, the convergence rates fall toward the expected asymptotic  $\mathcal{O}(h^{p+1})$  design order. Figure 5.13 also shows the time evolution of the errors for the various resolutions and one striking feature is the decay of the error over time for the fine grids. This is a phenomenon we do not fully understand.

**5.2.4.** Performance for singular solutions. To illustrate the behavior of the various schemes for more challenging problems in two dimensions, we briefly consider a problem with singular behavior due to both the initial conditions and the presence of piecewise constant wave speeds. The precise definition of the wave speeds is

$$c(x,y) = \begin{cases} .3 & \text{if } -0.9 \le x \le -0.1 \text{ and } .1 \le y \le .9, \\ .8 & \text{if } 0.1 \le x \le -0.1 \text{ and } .1 \le y \le .9, \\ .2 & \text{if } 0.1 \le x \le 0.9 \text{ and } -0.9 \le y \le -0.1, \\ .9 & \text{if } -0.9 \le x \le -0.1 \text{ and } -0.9 \le y \le -0.1, \\ 0.5 & \text{otherwise,} \end{cases}$$

and a graphical representation is shown in Figure 5.14. The initial conditions are taken as  $u_t(x, y, t = 0) = 0$ , and

| $L_h^2$ space-time error | ) |
|--------------------------|---|
|--------------------------|---|

| $(n_r, n_\theta, n_t)$ | Error                | Rate |
|------------------------|----------------------|------|
| (150, 450, 50000)      | $5.2 \times 10^{-4}$ |      |
| (200, 600, 100000)     | $1.5 \times 10^{-5}$ | 12.4 |
| (300, 900, 200000)     | $2.0 \times 10^{-7}$ | 10.6 |
| (400, 1200, 400000)    | $1.3 \times 10^{-8}$ | 9.6  |

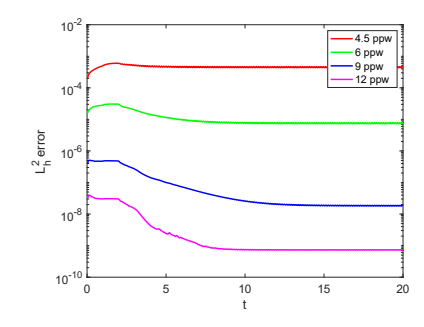


FIG. 5.13. Convergence with refinement for the cylinder scattering problem. Here  $n_r$ ,  $n_\theta$ , and  $n_t$  are the number of cells in the radial, azimuthal, and temporal domains, respectively. The error is computed using the relative  $L_h^2$  error in space-time, and the rate is the observed convergence rate based on two resolutions. At right are the errors versus time for the four simulations.

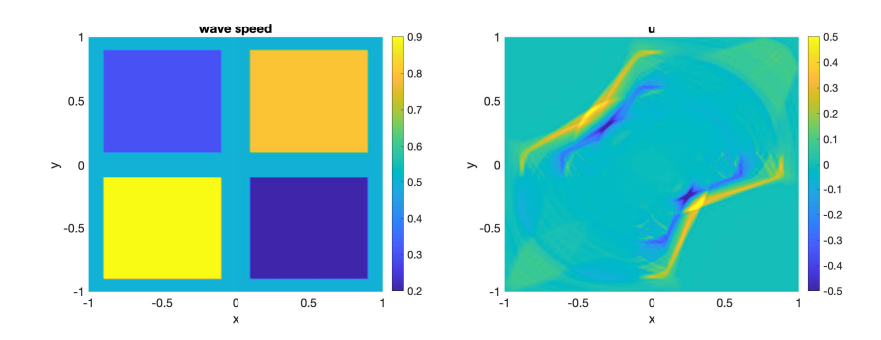


Fig. 5.14. At left is a color contour plot of the wave speeds. At right is the solution u computed using the SSIPG scheme with upwind flux, p=10,  $N_x=N_y=150$  grid points, and a final time of  $t_f=1.5$  (other methods yield largely similar results).

(5.14) 
$$u(x, y, t = 0) = \begin{cases} 1 & x^2 + y^2 < \frac{1}{10}, \\ 0 & \text{else}, \end{cases}$$

and the simulations are run to a final time t = 1.5. All physical boundary conditions are taken to be homogeneous Dirichlet.

Numerical results computed using p=10 with the SIPGD scheme, upwind fluxes, and the extrapolation closure are shown in Figure 5.14. One can clearly see the effect of the discontinuous wave speeds as the expanding wave has been accelerated or retarded along its path by faster or slower waves speeds, respectively. In order to clearly demonstrate the effect of upwind dissipation, Figure 5.15 presents  $u_t$  at the final time computed using SIPGD and IIPGD schemes with both the centered and upwind fluxes. Owing to the challenging nature of the problem, the solution itself contains propagating singularities, which interact with the discontinuous wave speeds to generate a rich set of reflected and transmitted waves. As discussed in section 5.1.2, the schemes react differently to the presence of solution singularities. This case is no different, and Figure 5.15 illustrates that the upwind flux is effective at removing spurious oscillations while simultaneously capturing the rich solution behavior, even for the nominally high-order accurate scheme implied by p=10. Similarly the symmetric schemes yield results with fewer spurious oscillations. These observations are entirely in agreement with the simpler 1D cases presented in section 5.1.2.

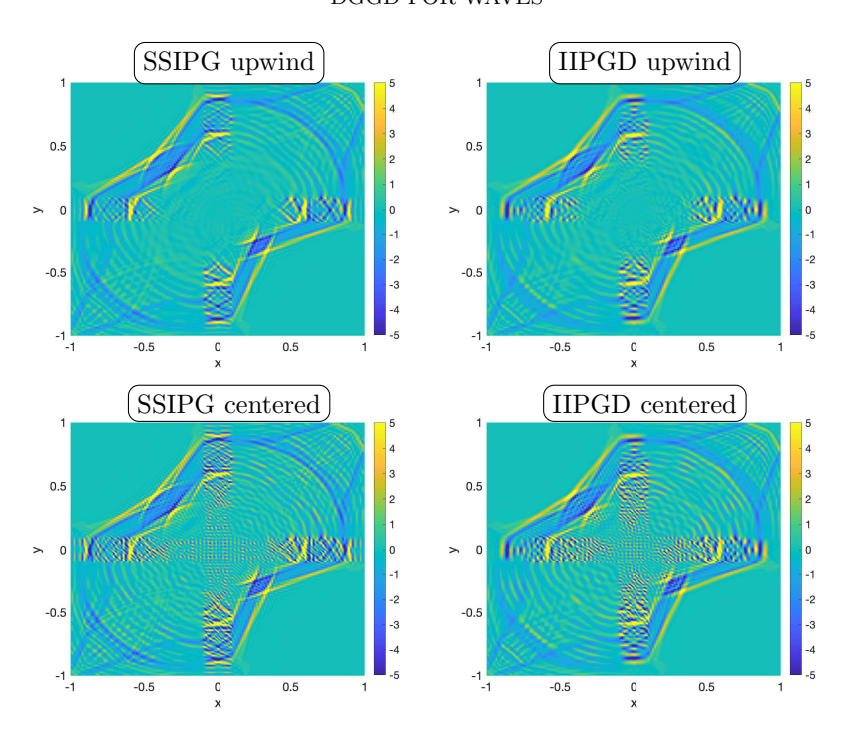


Fig. 5.15. Results for  $u_t$  at t = 1.5 with using p = 10,  $N_x = N_y = 150$  grid points, and a final time of  $t_f = 1.5$  using the various schemes. The effect of the upwind dissipation is clearly visible since spurious high-frequency oscillations have been suppressed. Similarly the symmetric schemes yield results with fewer spurious oscillations.

**6.** Conclusions. We have presented a new approach to GD applied to wave equations in their second-order formulation. As in all GD discretizations, the formulation is built around an underlying piecewise interpolant, which in this case is constructed on a dual grid. This construction results in discontinuities at the boundaries of the dual grid, and the corresponding basis functions are similarly discontinuous. Thus the inner product over the domain is formulated on the broken space and upon integration by parts leads to flux terms at the interelement boundaries. These flux terms are treated numerically using either centered or upwind, leading to energy conservative or energy dissipative schemes, respectively. We have formulated schemes as using both symmetric (SIPGD) and incomplete (IIPGD) penalty formulations, with the former found to yield a nodal superconvergence in many cases. In addition, we find that owing to the properties of the GD space, the usual penalty terms required to discretize the second-order operators with discontinuous spaces are not required. Analysis of the various schemes is performed, and the stability and convergence properties are presented. Finally, a detailed set of numerical experiments has been performed to support the theory and show the behavior of the discretizations across a range of potential scenarios.

There are a number of potential paths for future investigation. Given the observed superconvergence behavior, it is natural to pursue a similar interior penalty approach for higher-order operators, for example, those appearing in models of solid beams and plates. In addition, to increase the applicability of the methods we present, application of these approaches on more general grids, e.g., unstructured [26], overlapping, or hybrid grids [16], is something that should be addressed in more depth.

**Appendix A. Coercivity of bilinear form.** The stability of the IIPGD and SIPGD methods follows from the positivity of the bilinear form

(A.1) 
$$\sum_{l} \int_{x_{l-1/2}}^{x_{l+1/2}} c^2 w_x^2 + \tau \sum_{l} c^+ c^- w_x(x_{l+1/2}) \left( w(x_{l+1/2}^+) - w(x_{l+1/2}^-) \right),$$

where w is an arbitrary function in the GD space and  $\tau = 1, 2$ . Here we assume a uniform grid of width h, and by  $w_x(x_{l+1/2})$  we mean the unique left and right limit of  $w_x(x)$ . For completeness and to prepare for the coming calculations we prove this. Denote by  $w_\ell(x)$  the restriction of w to  $(x_{l-1/2}, x_{l+1/2})$ . Using the Newton form we can write for some degree p-1 polynomial  $\hat{w}_{l+1/2}(x)$  and constants  $c_l$ ,  $c_{l+1}$ 

$$w_l(x) = \hat{w}_{l+1/2}(x) + c_l \prod_{k=1-p/2}^{p/2} (x_l - kh),$$
  
$$w_{l+1}(x) = \hat{w}_{l+1/2}(x) + c_{l+1} \prod_{k=1-p/2}^{p/2} (x_l - kh).$$

As the degree-p correction terms are even with respect to  $x_{l+1/2}$  we have

$$\frac{dw_l}{dx}(x_{l+1/2}) = \frac{dw_{l+1}}{dx}(x_{l+1/2}) = \frac{d\hat{w}_{l+1/2}}{dx}(x_{l+1/2}).$$

We now specialize to the case of constant wave speed c and the  $x \in \mathbb{R}$ . (The calculations also apply in the periodic case or with compatibility boundary closures.) The linear operators which map the nodal data,  $w(x_l)$ , to the derivatives,  $w_x(x_{l+1/2})$ , and jumps,  $(w(x_{l+1/2}^+) - w(x_{l+1/2}^-))$ , are obviously translation-invariant and thus amenable to Fourier analysis. Denote these operators by D and J. Following, e.g., [25, Chap. 2], we can write

$$w(x_{l}) = \frac{1}{\sqrt{2\pi}} \int_{-\pi/h}^{\pi/h} e^{il\omega} \hat{w}(\omega) d\omega,$$

$$(A.2) \qquad Dw(x_{l+1/2}) = \frac{1}{\sqrt{2\pi}} \int_{-\pi/h}^{\pi/h} e^{i(l+1/2)\omega} \hat{D}(\omega) \hat{w}(\omega) d\omega,$$

$$Jw(x_{l+1/2}) = \frac{1}{\sqrt{2\pi}} \int_{-\pi/h}^{\pi/h} e^{i(l+1/2)\omega} \hat{J}(\omega) \hat{w}(\omega) d\omega.$$

Then by Parseval's relation

(A.3) 
$$h \sum_{l} Dw(x_{l+1/2}) Jw(x_{l+1/2}) = \int_{-\pi/h}^{\pi/h} \bar{\hat{D}}(\omega) \hat{J}(\omega) |\hat{w}(\omega)|^2 d\omega.$$

From (A.3) we conclude as follows.

LEMMA A.1. If  $\hat{D}(\omega)\hat{J}(\omega) \geq 0$  for all  $\omega \in (-\pi/h, \pi/h)$ , then  $\sum_{l} Dw(x_{1+1/2})$   $Jw(x_{l+1/2}) \geq 0$  and therefore (A.1) is nonnegative.

The symbols  $\hat{D}(\omega)$  and  $\hat{J}(\omega)$  defined in (A.2) are easily calculated and thus the positivity of  $\hat{D}(\omega)\hat{J}(\omega)$  can be checked for any p; we have done so for p < 100 and found

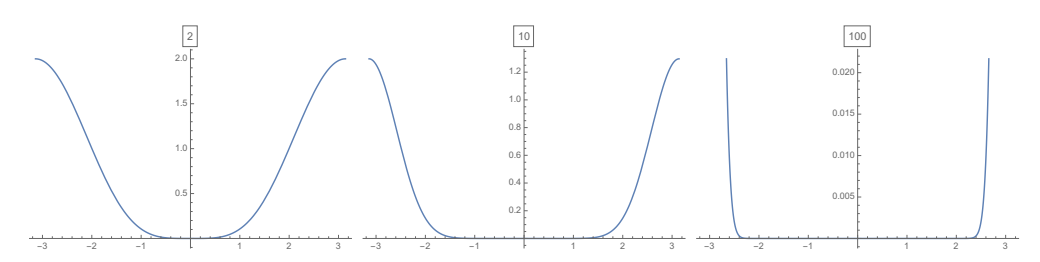


Fig. A.1. Plots of  $\hat{D}(\omega) \cdot \hat{J}(\omega)$  for p = 2, 10, 100.

that the hypothesis of the lemma holds, establishing the fact that the bilinear form is nonnegative in these cases. We note that both  $\hat{D}(\omega)$  and  $\hat{J}(\omega)$  are purely imaginary, and so we need only check that the imaginary parts have the same sign. The staggered difference operators D are well-known not to have an imaginary part which never changes sign except at  $\omega=0$  and since the jump operator also approximates the (scaled) derivative the sign will be the same for  $\omega$  small. Thus the result holds so long as the only Fourier mode for which the jump operator is zero is the constant mode, which we find to be true. Indeed, if the jumps are zero w is a polynomial, and the only periodic polynomial is a constant. We show in Figure A.1 plots of  $\hat{D}(\omega) \cdot \hat{J}(\omega)$  for p=2,10,100.

### REFERENCES

- D. APPELÖ AND T. HAGSTROM, A new discontinuous Galerkin formulation for wave equations in second-order form, SIAM J. Numer. Anal., 53 (2015), pp. 2705–2726.
- B. VAN LEER, Towards the ultimate conservative difference scheme, V. A second-order sequel to Godunov's method, J. Comput. Phys., 32 (1979), pp. 101-136.
- [3] G. A. Baker, Error estimates for finite element methods for second order hyperbolic equations, SIAM J. Numer. Anal., 13 (1976), pp. 564-576, https://doi.org/10.1137/0713048.
- [4] J. W. Banks and T. Hagstrom, On Galerkin difference methods, J. Comput. Phys., 313 (2016), pp. 310–327.
- [5] J. W. Banks, T. Hagstrom, and J. Jacangelo, Galerkin differences for acoustic and elastic wave equations in two space dimensions, J. Comput. Phys., 372 (2018), pp. 864–892.
- [6] J. W. Banks and W. D. Henshaw, Upwind schemes for the wave equation in second-order form, J. Comput. Phys., 231 (2012), pp. 5854–5889.
- [7] J. P. Boris and D. L. Book, Flux-corrected transport. I. SHASTA, a fluid transport algorithm that works, J. Comput. Phys., 11 (1973), pp. 38–69.
- [8] B. COCKBURN AND C. W. Shu, TVB Runge-Kutta local projection discontinuous Galerkin finite-element method for conservation-laws 2: general framework, Math. Comp., 52 (1989), pp. 411–435.
- [9] P. COLELLA AND P. R. WOODWARD, The piecewise parabolic method (PPM) for gas-dynamical simulations, J. Comput. Phys., 54 (1984), pp. 174–201.
- [10] M. Dumbser, D. Balsara, E. F. Toro, and C. D. Munz, A unified framework for the construction of one-step finite volume and discontinuous Galerkin schemes on unstructured meshes, J. Comput. Phys., 227 (2008), pp. 8209–8253.
- [11] S. K. Godunov, Finite difference method for numerical computation of discontinuous solutions of the equations of fluid dynamics, Mat. Sb., 47 (1959), pp. 271–306.
- [12] M. J. GROTE, A. SCHNEEBELI, AND D. SCHÖTZAU, Discontinuous galerkin finite element method for the wave equation, SIAM J. Numer. Anal., 44 (2006), pp. 2408–2431, https://doi.org/ 10.1137/05063194X.
- [13] A. HARTEN, B. ENGQUIST, S. OSHER, AND S. CHAKRAVARTHY, Uniformly high order accurate essentially non-oscillitory schemes, III, J. Comput. Phys., 71 (1987), pp. 231–303.
- [14] J. JACANGELO, J. W. BANKS, AND T. HAGSTROM, Galerkin differences for high-order partial differential equations, SIAM J. Sci. Comput., 42 (2020), pp. B447–B471.
- [15] G.-S. JIANG AND C.-W. SHU, Efficient implementation of weighted ENO schemes, J. Comput. Phys., 126 (1996), pp. 202–228.

- [16] J. E. KOZDON, L. C. WILCOX, T. HAGSTROM, AND J. W. BANKS, Robust approaches to handling complex geometries with galerkin difference methods, J. Comput. Phys., 392 (2018), pp. 483–510.
- [17] S. Lele, Compact finite difference schemes with spectral-like resolution, J. Comput. Phys., 103 (1992), pp. 16–42.
- [18] L. LI, J. LOU, AND H. LUO, A reconstructed discontinuous Galerkin method based on variational reconstruction for compressible flows, in Proceedings of the 10th International Conference on Computational Fluid Dynamics, 2018, ICCFD10-140.
- [19] R. LI, P. MING, Z. SUN, AND Z. YANG, An arbitrary-order discontinuous Galerkin method with one unknown per element, J. Sci. Comput., 80 (2018), pp. 268–288, https://doi.org/10. 1007/s10915-019-00937-y.
- [20] P. Martin, Multiple Scattering: Interaction of Time-Harmonic Waves with N Obstacles, Cambridge University Press, Cambridge, UK, 2006.
- [21] S. MIZOHATA, The Theory of Partial Differential Equations, Cambridge University Press, Cambridge, UK, 1973.
- [22] B. RIVIERE, Discontinuous Galerkin Methods for Solving Elliptic and Parabolic Equations: Theory and Implementation, Frontiers in Appl. Math. 35, SIAM, Philadelphia, 2008.
- [23] B. RIVIERE AND M. WHEELER, Discontinuous finite element methods for acoustic and elastic wave problems, Contemp. Math., 329 (2003), pp. 271–282.
- [24] M. SHOUCRI AND G. KNORR, Numerical integration of the Vlasov equation, J. Comput. Phys., 14 (1974), pp. 84–92.
- [25] J. STRIKWERDA, Finite Difference Schemes and Partial Differential Equations, SIAM, Philadelphia, 2004.
- [26] G. Yan, S. Kaur, J. E. Hicken, and J. W. Banks, Entropy-stable Galerkin difference discretization on unstructured grids, AIAA Aviation 2020 Forum, https://doi.org/10.2514/6. 2020-3033.